RESEARCH ARTICLE

Targeting tankyrase scaffolding in the β-catenin destruction complex by PROTAC overcomes the limitation of catalytic inhibitors in colorectal cancer

Qian Wang[1], Liping Li[1], Lin You[1], Shuai Wang[1], Lei Han[1], Bingnan Wang[1], Liping Yao[1], Yesu Addepalli[1], Yong Lu[1], Ilgen Mender[2], Ann M Flusche[2], Chiho Kim[1†], Nageswari Yarravarapu[2], Andrew Lemoff[1], Lawrence Lum[2‡], Jerry W Shay[2], Yonghao Yu[1†], Chuo Chen[1*]

[1]Department of Biochemistry, UT Southwestern Medical Center, Dallas, United States; [2]Department of Cell Biology, UT Southwestern Medical Center, Dallas, United States

***For correspondence:** Chuo.Chen@utsouthwestern.edu

Present address: †Department of Molecular Pharmacology and Therapeutics, Columbia University Vagelos College of Physicians and Surgeons, New York, New York, United States; ‡Apertor Pharmaceuticals, South San Francisco, United States

Competing interest: See page 22

Funding: See page 22

Preprint posted
24 September 2025
Sent for Review
20 September 2025
Reviewed preprint v1
18 November 2025
Reviewed preprint v2
21 July 2026
Reviewed preprint v3
03 August 2026
Version of Record
04 November 2026

Reviewing Editor: Roel Nusse, Stanford University, United States

© Copyright Wang *et al*. This article is distributed under the terms of the Creative Commons Attribution License, which permits unrestricted use and redistribution provided that the original author and source are credited.

eLife Assessment

This **important** study reports the development of the first tankyrase degrader and demonstrates its enhanced ability to inhibit β-catenin signaling compared to conventional tankyrase inhibitors. The evidence supporting the conclusions is comprehensive and **convincing**, based on rigorous biochemical and cellular analyses. The findings will be of broad interest to researchers studying Wnt signaling, protein degradation, and cancer biology.

Abstract Aberrant WNT/β-catenin signaling drives tumorigenesis and metastasis in cancer. Although enzymatic inhibitors of tankyrase (TNKS) effectively block AXIN degradation and stabilize the β-catenin destruction complex (DC), they have demonstrated limited efficacy in various colorectal cancer (CRC) models. Here, we demonstrate that, unexpectedly, the induction of AXIN puncta represents a major barrier to achieving therapeutic efficacy. Mechanistically, catalytic inhibition of TNKS prevents TNKS turnover and drives its accumulation in the DC, wherein the scaffolding function of TNKS induces AXIN puncta formation, rigidifies the DC, and impedes β-catenin turnover. Chemically induced degradation of TNKS overcomes this limitation by stabilizing AXIN without puncta formation, providing a deeper suppression of the WNT/β-catenin pathway activity and the proliferation of CRC cells harboring dysfunctional APC mutations. Collectively, these findings provide an explanation for the unsatisfactory outcomes of drugging the WNT/β-catenin signaling pathway by TNKS inhibitors and highlight TNKS degradation as a promising approach to treat WNT/β-catenin-driven CRC.

Introduction

WNT/β-catenin signaling plays an important role in cell growth, differentiation, and migration (***Nusse and Clevers, 2017***; ***Clevers and Nusse, 2012***). Dysregulation of this pathway enables reprogrammed cancer cells to proliferate, metastasize, and resist chemo- and radiotherapies. In colorectal cancer (CRC), loss-of-function mutations in adenomatous polyposis coli (APC) are the major drivers of aberrant WNT/β-catenin signaling (***Zhang and Shay, 2017***). However, therapeutic targeting of this oncogenic pathway remains unsuccessful despite extensive efforts (***Zhong and Virshup, 2020***). For example,

although silencing tankyrase (TNKS1/2, also known as PARP5A/B and ATRD5/6 and encoded by *TNKS* and *TNKS2*, collectively referred to as TNKS hereafter) (**Hsiao and Smith, 2008**; **Haikarainen et al., 2014**; **Mariotti et al., 2017**) phenocopied APC restoration and prevented tumorigenesis in *APC*-null mice (**Schatoff et al., 2019**), TNKS inhibitors (TNKSi) failed to show promising efficacy in various in vitro and in vivo CRC models. Addressing the discrepancy between the genetic and pharmacological interception of WNT/β-catenin signaling through TNKS may provide a path toward developing new CRC treatments.

The axis inhibition protein (AXIN) and APC are both scaffolding proteins of the β-catenin destruction complex (DC) that likely exists as biomolecular condensates in the cytoplasm to prime β-catenin for proteasomal degradation (**Schaefer and Peifer, 2019**; **Bienz, 2020**; **Gammons and Bienz, 2018**). As TNKS-catalyzed poly(ADP-ribose)-dependent ubiquitination (PARdU) is required for the turnover of AXIN (**Huang et al., 2009**; **Zhang et al., 2011**; **DaRosa et al., 2015**), blocking the enzymatic function of TNKS by IWR1 or XAV939 leads to AXIN accumulation (**Huang et al., 2009**; **Chen et al., 2009**), thereby enhancing the ability of the DC to promote β-catenin degradation. The accompanied AXIN puncta formation is generally attributed to AXIN accumulation and is considered to play a positive role in suppressing WNT/β-catenin signaling. However, TNKS also associates with the DC (**de la Roche et al., 2014**; **Thorvaldsen et al., 2015**; **Martino-Echarri et al., 2016**), where its contributions to the DC function remain poorly understood. Specifically, because TNKS regulates its own abundance through self-poly(ADP-ribosylation) (PARylation), catalytic inhibition also promotes drastic TNKS accumulation (**Huang et al., 2009**). It is unclear whether this feedback mechanism affects the DC function and results in the limited anticancer efficacy of TNKSi, as inhibitor-induced TNKS accumulation may support WNT/β-catenin signaling through molecular scaffolding independently of its catalytic function. Indeed, deletion of the catalytic PARP domain of TNKS attenuated, but did not fully suppress the WNT-induced transcription of the TCF/LEF-controlled genes (**Huang et al., 2009**; **de la Roche et al., 2014**; **Mariotti et al., 2016**). By contrast, removal of the sterile alpha motif (SAM) domain or the ankyrin repeat clusters (ARCs) of TNKS abolished the WNT/β-catenin pathway activity more completely.

To understand the role of TNKS scaffolding in WNT/β-catenin signaling, we developed a TNKS-targeting proteolysis-targeting chimera (PROTAC) (**Schreiber, 2021**; **Chirnomas et al., 2023**) as a selective TNKS degrader (TNKSd). Comparison between TNKSd and TNKSi allowed us to understand the catalysis-independent scaffolding function of TNKS and uncover the mechanism underlying the ineffectiveness of TNKSi against cancers. We found that inhibiting TNKS by TNKSi led to the accumulation of TNKS within the DC, which induced AXIN puncta formation, promoted maturation (**Shin and Brangwynne, 2017**; **Banani et al., 2017**) of the DC condensates, and impeded β-catenin turnover. In contrast, degrading TNKS by TNKSd enriched AXIN without inducing puncta or impairing the dynamics of the DC. As a result, TNKSd provided deeper suppression of the WNT/β-catenin pathway activity as well as better control of the proliferation of CRC cells harboring dysfunctional APC mutations. Collectively, our study provides new insights into the roles of TNKS in the DC and presents a promising strategy to enhance the therapeutic efficacy of TNKS-targeting anticancer treatments.

Results

IWR1-POMA induces TNKS degradation

To study the role of TNKS scaffolding, we first developed a PROTAC molecule to enable selective degradation of TNKS1 and TNKS2 at the same time by small molecules. Compared to conventional genetic approaches, this chemical approach helps address gene redundancy more conveniently and effectively. TNKS uses nicotinamide adenine dinucleotide (NAD^+) as the ADP-ribose donor. The corresponding pocket in the PARP domain contains two discrete sites, one for nicotinamide (NI) and the other for adenosine (AD) binding. IWR1 is a highly selective TNKSi that exploits the AD site unique to TNKS, and IWR6 is a promiscuous but potent TNKSi structurally similar to XAV939 that binds to the NI site common to all PARPs (**Huang et al., 2009**; **Kulak et al., 2015**). Based on the crystal structures of TNKS1 and TNKS2 in complex with IWR1 or XAV939 (***Figure 1—figure supplement 1***), we envisioned that modifying the quinoline group of IWR1 and the phenyl group of IWR6 would not negatively impact TNKS-binding. We have thus created a small library of 30 PROTAC molecules by attaching pomalidomide (**Winter et al., 2015**) or VH032 (**Galdeano et al., 2014**) through a PEG chain

of various lengths to IWR1 or IWR6 (***Figure 1—figure supplement 2A***) for engaging cereblon (CRBN) or the von Hippel–Lindau tumor suppressor protein (VHL), respectively, and examined their ability to induce TNKS degradation.

To facilitate the discovery of a TNKSd, we also developed a luciferase assay to measure the level of TNKS1 in a high-throughput manner. Using the CRISPR-assisted insertion tagging (CRISPaint) technology (***Schmid-Burgk et al., 2016***), we introduced a nanoluciferase (NanoLuc) tag to the C-terminus of TNKS1 in HAP1 cells (***Figure 1—figure supplement 2B***). We chose to monitor TNKS1 because it is constitutively expressed while TNKS2 is expressed minimally under basal conditions. By following the luciferase activity, the knockdown efficiency of all five series of the PROTAC molecules could be quantified easily and accurately using a robotic liquid dispenser system in 96-well plates, which significantly improved the efficiency over the traditional method that relies on western blotting and image processing. Using this luciferase assay, we found that the IWR1-based PROTACs eliminated TNKS1 significantly more effectively than the IWR6-based PROTACs (***Figure 1—figure supplement 2C***). Additionally, CRBN mediated TNKS1 degradation more efficiently than VHL. Inserting a triazole group between the quinoline group and the PEG chain further enhanced the degradation efficiency. However, replacing the PEG linker with a nonpolar or rigid linker did not improve the efficacy, and employing G007-LK (***Lau et al., 2013***) as the warhead with various linker strategies led to reduced potency and degree of degradation (***Figure 1—figure supplement 2D***).

IWR1-TP4-Poma (IWR1-POMA hereafter) is the most potent PROTAC among these series. It initiated TNKS1 degradation at 1 nM, operated with a DC_{50} value of 60 nM, and reached 96% degradation at 1.2 μM in HAP1 cells (***Figure 1A***). Western blot analysis confirmed that IWR1-POMA could also deplete TNKS1 and suppress the induction of TNKS2 in a dose- and time-dependent manner in DLD-1 CRC cells that carry truncating APC mutations (***Figure 1B and C***). The level of TNKS did not recover 36 h after IWR1-POMA was removed, indicating a durable drug effect (***Figure 1—figure supplement 3A***). Addition of IWR1, pomalidomide, or MG132 blocked TNKS degradation (***Figure 1—figure supplement 3B and C***), supporting that IWR1-POMA functioned through the designed mode of action. The generality of IWR1-POMA to induce TNKS degradation was demonstrated in SW480, HT-29, and HeLa cells (***Figure 1—figure supplement 3D***). The ability of IWR1-POMA to stabilize AXIN and promote β-catenin degradation in the cytoplasm was confirmed further in HEK293 cells (***Figure 1D***). Compared to IWR1, IWR1-POMA provided better control of the cytosolic β-catenin level. The performance of this PROTAC molecule is particularly notable, considering that shutting down the catalysis of TNKS leads to a >30-fold accumulation of total TNKS, creating a nearly three-orders-of-magnitude difference in the levels of TNKS between catalytic inhibition and chemically induced degradation. Although the hook effect was observed at high concentrations, presumably due to the formation of nonproductive binary protein-ligand complexes under these conditions, to our knowledge, this is the first example of targeted degradation of an auto-regulated protein.

To confirm the ability of IWR1-POMA to engage TNKS, we prepared IWR1-PEG3-NCT as a bioluminescence resonance energy transfer (BRET) tracer (***Figure 1—figure supplement 3E***; ***Robers et al., 2015***). We then treated HAP1-TNKS1-NanoLuc cells with MG132 to increase the signal-to-noise ratio and to normalize the TNKS level in the presence of IWR1 and IWR1-POMA. Addition of IWR1 effectively reduced the BRET signals; however, the intrinsic fluorescence (***Kampmann et al., 2015***) of IWR1-POMA prevented the assessment of its binding affinity by this method. Nonetheless, the observation of significant BRET signals of IWR1-POMA at high concentrations prompted us to test whether it could be used directly as a BRET acceptor for NanoLuc despite poor spectral overlap (***Weihs et al., 2020***). Indeed, the BRET signals increased in a dose-dependent manner after adding IWR1-POMA to HAP1-TNKS1-NanoLuc cells in the presence of MG132 (***Figure 1—figure supplement 3F***). Accordingly, we titrated IWR1 into HAP1-TNKS1-NanoLuc cell in the presence of 0.5 μM of IWR1-POMA and found that IWR1 suppressed the BRET signals with an IC_{50} value of 0.25 μM (***Figure 1—figure supplement 3G***). Repeating this experiment in 293T cells transfected with TNKS1-NanoLuc plasmid improved the BRET signal-to-noise ratio and confirmed that the pomalidomide chromophore can be used as a BRET pair for NanoLuc. It also confirmed that IWR1-POMA (0.5 μM) binds to TNKS1 with a slight reduction in affinity as compared to IWR1 (IC_{50} 0.15 μM).

To examine the degradation specificity of IWR1-POMA, we performed proteome-wide expression profiling on DLD-1 cells treated with DMSO, IWR1, or IWR1-POMA for 16 h. Using a tandem mass tag (TMT)-based, multiplexed quantitative mass spectrometric (MS) approach with two biologically

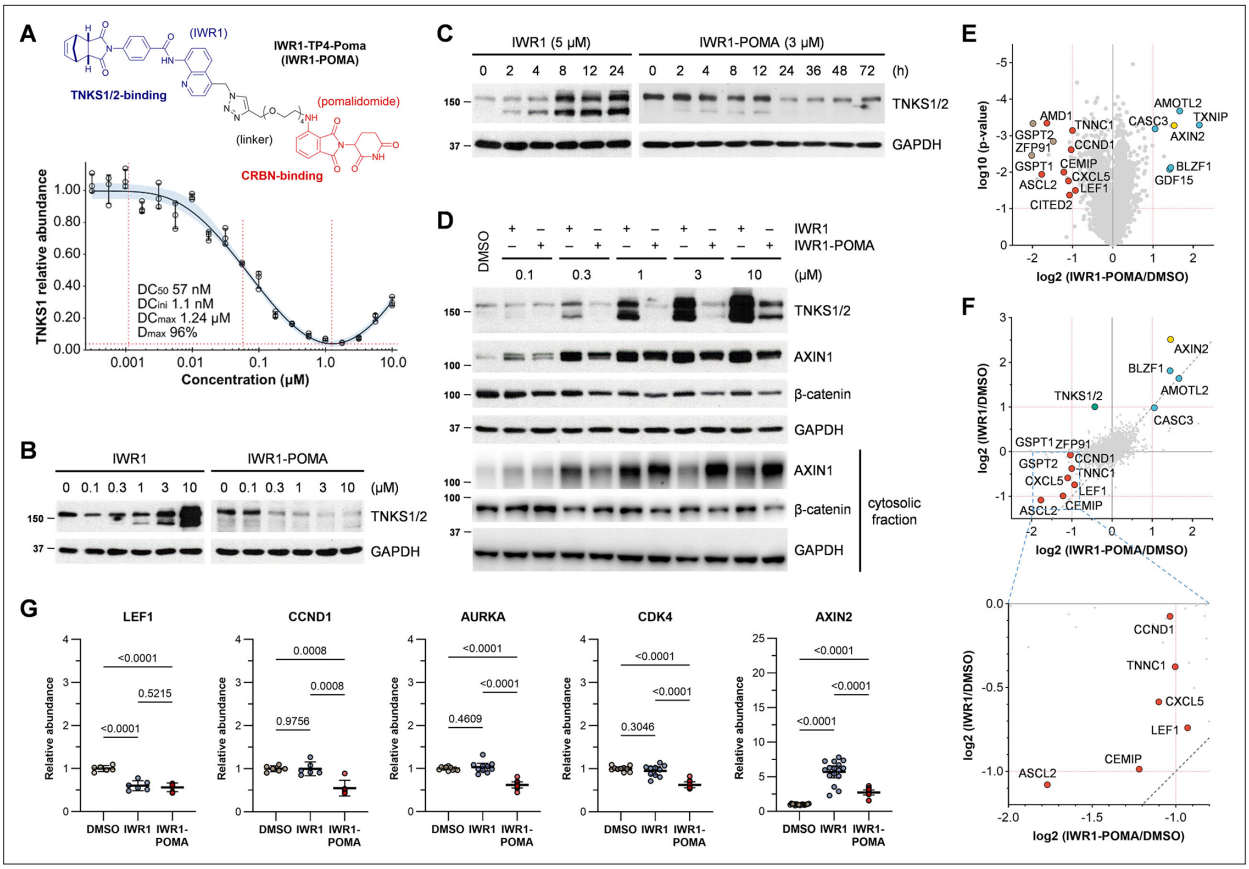


Figure 1. Characterization of IWR1-POMA. (**A**) IWR1-POMA induced TNKS degradation with a DC_{50} value of 60 nM and reached a nearly complete depletion of TNKS1 at 1.2 μM in HAP1 cells. The dose–response curve is presented as mean ± SEM (n=3 biological samples) with 95% confidence interval (CI) indicated by the shaded area. (**B, C**) IWR1 induced massive TNKS accumulation while IWR1-POMA promoted deep degradation in a dose- and time-dependent manner in DLD-1 cells. (**D**) IWR1-POMA promoted a more complete degradation of β-catenin than IWR1 in HEK293 cells cultured with Wnt3A conditioned media. (**E**) Volcano plot of the TMT experiment results. TNKS substrates (light blue) accumulated and WNT/β-catenin-regulated proteins (red) downregulated in DLD-1 cells treated with IWR1-POMA (3 μM). AXIN2 (yellow) is both a TNKS substrate and a WNT target. GSPT1/2 and ZFP91 (light brown) are the only off-targets identified. (**F**) Comparative analysis of the TMT experiment showing that the levels of several WNT/β-catenin regulated proteins (red) were preferentially reduced by IWR1-POMA relative to IWR1 treatment. The dashed line denotes equal protein abundance between the two treatments. Data points above this line in Quadrant III represent proteins selectively downregulated by IWR1-POMA relative to IWR1. (**G**) Relative peptide abundances of selected WNT targets in the TMT experiment with p-values calculated by two-tailed unpaired *t*-test.

The online version of this article includes the following source data and figure supplement(s) for figure 1:

Source data 1. PDF files for western blot analysis displayed in ***Figure 1***.

Source data 2. Original files for western blot analysis displayed in ***Figure 1B***.

Source data 3. Original files for western blot analysis displayed in ***Figure 1C***.

Source data 4. Original files for western blot analysis displayed in ***Figure 1D***.

Source data 5. Original files for western blot analysis displayed in ***Figure 1D***.

Figure supplement 1. Crystal structures used to guide the design of PROTAC molecules.

Figure supplement 2. Identification of active PROTAC molecules using CRISPR-engineered HAP1 cells expressing a TNKS1-NanoLuc fusion protein.

Figure supplement 3. Additional characterization of IWR1-POMA.

Figure supplement 3—source data 1. PDF files for western blot analysis displayed in ***Figure 1—figure supplement 3***.

Figure supplement 3—source data 2. Original files for western blot analysis displayed in ***Figure 1—figure supplement 3A, B***.

Figure supplement 3—source data 3. Original files for western blot analysis displayed in ***Figure 1—figure supplement 3D***.

Figure supplement 4. Proteomic analysis of DLD-1 cells treated with DMSO, IWR1, or IWR1-POMA.

Figure supplement 4—source data 1. PDF file for western blot analysis displayed in ***Figure 1—figure supplement 4A***.

Figure supplement 4—source data 2. Original file for western blot analysis displayed in ***Figure 1—figure supplement 4A***.

independent replicate samples (***Figure 1—figure supplement 4A***), we identified 7884 proteins, among which 5822 could be quantified with high confidence (<1% FDR). Correlation analysis confirmed the consistency of the quantitative analysis of the two biological replicates (***Figure 1—figure supplement 4B***). However, accurate quantification of TNKS1 proved challenging, as only a low-abundance peptide corresponding to TNKS1 was detected in this experiment. Nonetheless, IWR1-POMA induced the accumulation of AXIN2 along with other TNKS substrates (***Figure 1E***). LEF1 and several other WNT targets were also effectively downregulated, confirming the on-target drug effects. Pairwise binary comparison of the drug treatment versus control indicated better control of WNT signaling by IWR1-POMA in addition to high degradation specificity (***Figure 1F and G***). GSPT1/2 and ZFP91, three common off-targets of the IMiD-based PROTACs, were the only perturbations not related to the WNT pathway. None of the other 7 PARPs and 81 NAD^+/$NADP^+$-dependent enzymes identified in this MS experiment were significantly affected by IWR1-POMA (***Figure 1—figure supplement 4C***).

PROTAC suppresses catalysis-independent WNT/β-catenin signaling by TNKS

A previous study showed that polymerization of PARylation-incompetent TNKS can drive WNT/β-catenin signaling (***Mariotti et al., 2016***). To understand whether the lack of efficacy of TNKSi in suppressing CRC cell growth originated from the PARylation-independent WNT/β-catenin signaling induced by the accumulated TNKS upon catalytic inhibition, we treated Wnt3A-stimulated 293T cells with IWR1 or IWR1-POMA. We reason that, by removing both the catalysis-dependent and independent functions of TNKS, IWR1-POMA may suppress WNT/β-catenin signaling more completely than IWR1 that inhibits AXIN PARylation but also promotes TNKS accumulation and polymerization. Indeed, IWR1-POMA promoted β-catenin degradation significantly more effectively than IWR1 under various doses of Wnt3A (***Figure 2—figure supplement 1A***). To investigate the individual contribution of TNKS1 and TNKS2 to WNT/β-catenin signaling, we co-transfected a low dose of TNKS1 plasmid together with SuperTopFlash (STF), a luciferase reporter for the WNT/β-catenin activity, into 293T-TNKS1/2-DKO cells wherein both TNKS1 and TNKS2 were deleted by CRISPR (***Bhardwaj et al., 2017***; ***Figure 2—figure supplement 1B***). We found that the addition of IWR1 suppressed the TNKS1-induced STF activity but not completely (***Figure 2A***, ***Figure 2—figure supplement 1C***). There was a small but noticeable residual activity, which could not be removed by increasing the concentration of IWR1. In contrast, IWR1-POMA induced TNKS1 degradation and promoted deeper suppression of the STF activity. Similarly, IWR1-POMA reduced the level of TNKS2 and provided better control of the STF activity than IWR1 in TNKS1/2-DKO cells expressing TNKS2 (***Figure 2B***, ***Figure 2—figure supplement 1D***). As such, both TNKS1 and TNKS2 can contribute to WNT signaling that persists even in the presence of catalytic inhibition of TNKS PARylation.

We next used PARylation-incompetent variants of TNKS to verify whether TNKS1 and TNKS2 can promote WNT/β-catenin signaling independently of their catalytic function. The catalytic site of TNKS is highly conserved. Deactivation of the H-Y-E triad of TNKS1 with H1184A and E1291A mutations (***Cook et al., 2002***) abolishes the binding of NAD^+ and the accepting ADP ribose. This PARP-dead (PD) variant induced notable WNT/β-catenin signaling in the TNKS1/2-DKO cells even at low doses, confirming that TNKS1 has a catalysis-independent functional role in the DC (***Figure 2C***, ***Figure 2—figure supplement 1E***). Addition of IWR1-POMA degraded TNKS1-PD and reduced the pathway activity, whereas treatment with IWR1 had no effect. Similarly, TNKS2-M1054V having an impaired ability to interact with the accepting ADP ribose (***Sbodio et al., 2002***) induced robust WNT/β-catenin signaling and was insensitive to IWR1 treatment (***Figure 2D***, ***Figure 2—figure supplement 1F***). In contrast, IWR1-POMA degraded this catalytically inactive variant of TNKS2 and suppressed the corresponding STF activity in a dose-dependent manner. Collectively, these data support the hypothesis that both TNKS1 and TNKS2 play an additional role in the DC to regulate WNT/β-catenin signaling through a mechanism beyond catalytic PARylation of AXIN (***Mariotti et al., 2016***). Degradation of TNKS eliminates both the enzymatic and non-enzymatic activities of TNKS, providing better control of the WNT/β-catenin signaling than catalytic inhibition (***Figure 2—figure supplement 1G***).

Tankyrase controls the dynamic assembly of the DC

AXIN interacts with APC to work as a molecular scaffold for the DC to catalyze β-catenin phosphorylation and ubiquitination. TNKS also associates with this complex (***de la Roche et al., 2014***; ***Thorvaldsen***

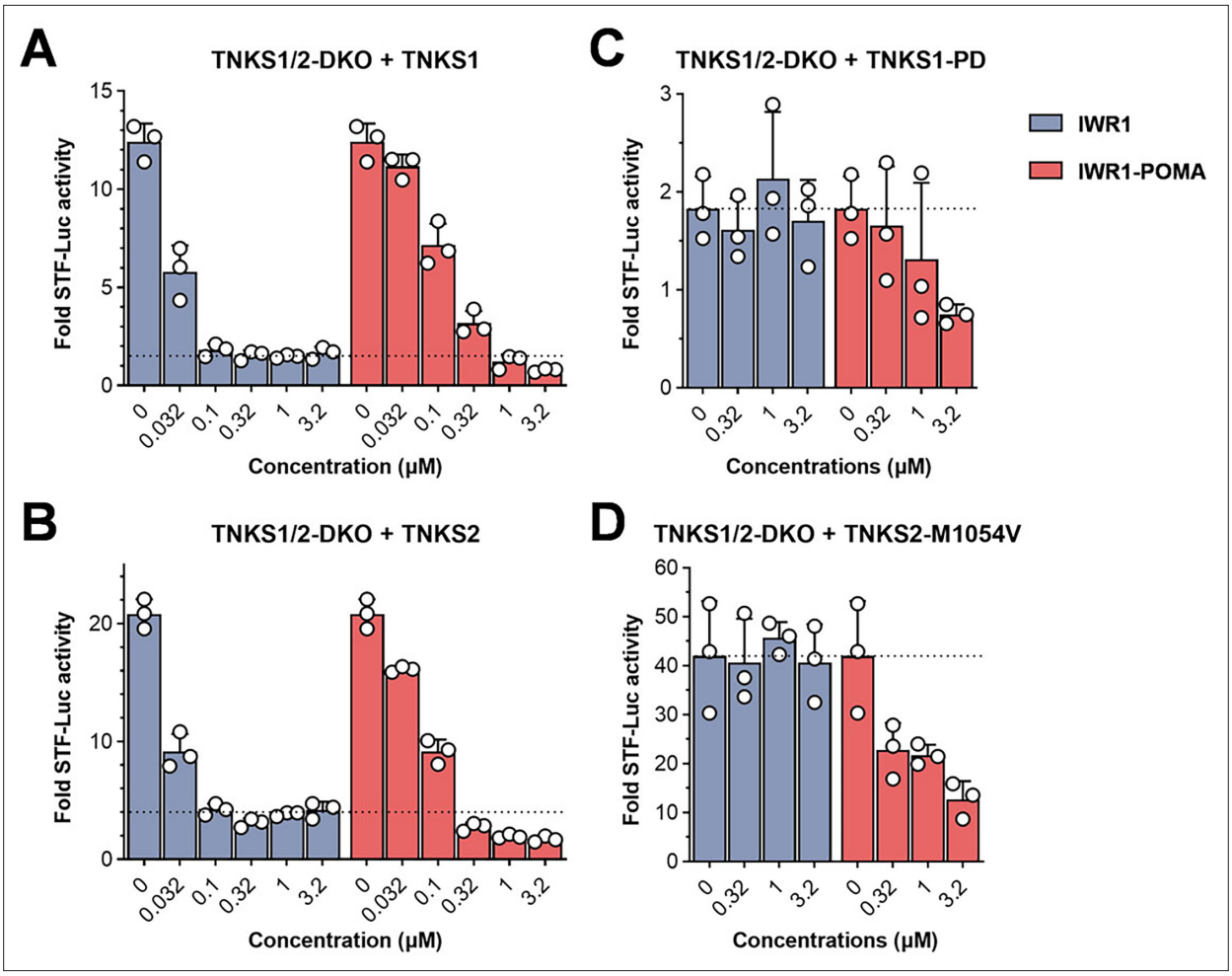


Figure 2. IWR1-POMA degraded TNKS to suppress both catalysis-dependent and independent WNT signaling. (**A**) 293T-TNKS1/2-DKO cells were transfected with FLAG-TNKS1 and STF plasmids and then treated with IWR1 or IWR1-POMA. In contrast to IWR1 that plateaued in suppressing the WNT/β-catenin signaling induced by TNKS1, IWR1-POMA allowed for a more complete control of the pathway activity. (**B**) 293T-TNKS1/2-DKO cells transfected with FLAG-TNKS2 and STF plasmids and then treated with IWR1 or IWR1-POMA similarly showed that catalytic inhibition led to residual WNT/β-catenin activity. (**C**) 293T-TNKS1/2-DKO cells were transfected with 3×FLAG-TNKS1-PD and STF plasmids and then treated with IWR1 or IWR1-POMA. IWR1-POMA suppressed the luciferase activities whereas IWR1 had no effect. (**D**) 293T-TNKS1/2-DKO cells transfected with FLAG-TNKS2-M1054V and STF plasmids and then treated with IWR1 or IWR1-POMA. TNKS2 exhibited robust scaffolding effects. All data are presented as mean ± SEM (n=3 biological samples).

The online version of this article includes the following source data and figure supplement(s) for figure 2:

Figure supplement 1. Degradation of TNKS by IWR1-POMA in 293T cells.

Figure supplement 1—source data 1. PDF files for western blot analysis displayed in ***Figure 2—figure supplement 1***.

Figure supplement 1—source data 2. Original files for western blot analysis displayed in ***Figure 2—figure supplement 1***.

et al., 2015; ***Martino-Echarri et al., 2016***) to control the AXIN level. Although much is known about the catalytic function of TNKS, its scaffolding function (***Mariotti et al., 2016***; ***Riccio et al., 2016***) is poorly understood. To study the non-enzymatic function of TNKS in WNT signaling, we transfected 293T cells with a low dose of AXIN1-mCherry plasmid and confirmed that TNKS colocalized with AXIN1 to form micrometer-sized puncta (***Figure 3A***, ***Figure 3—figure supplement 1***). In contrast, in TNKS1/2-DKO cells that lack TNKS, AXIN1-mCherry distributed diffusely throughout the cytoplasm as small aggregates (***Figure 3B***). However, AXIN puncta formed readily when AXIN1-mCherry was expressed together with TNKS1 in the TNKS1/2-DKO cells (***Figure 3C***). Similarly, TNKS2 also induced AXIN puncta in TNKS1/2-DKO cells (***Figure 3D***), suggesting that TNKS1 and TNKS2 play a redundant structural role in the DC to support AXIN puncta formation. To further verify whether AXIN PARylation is involved in the puncta formation, we expressed AXIN1-mCherry together with catalytically

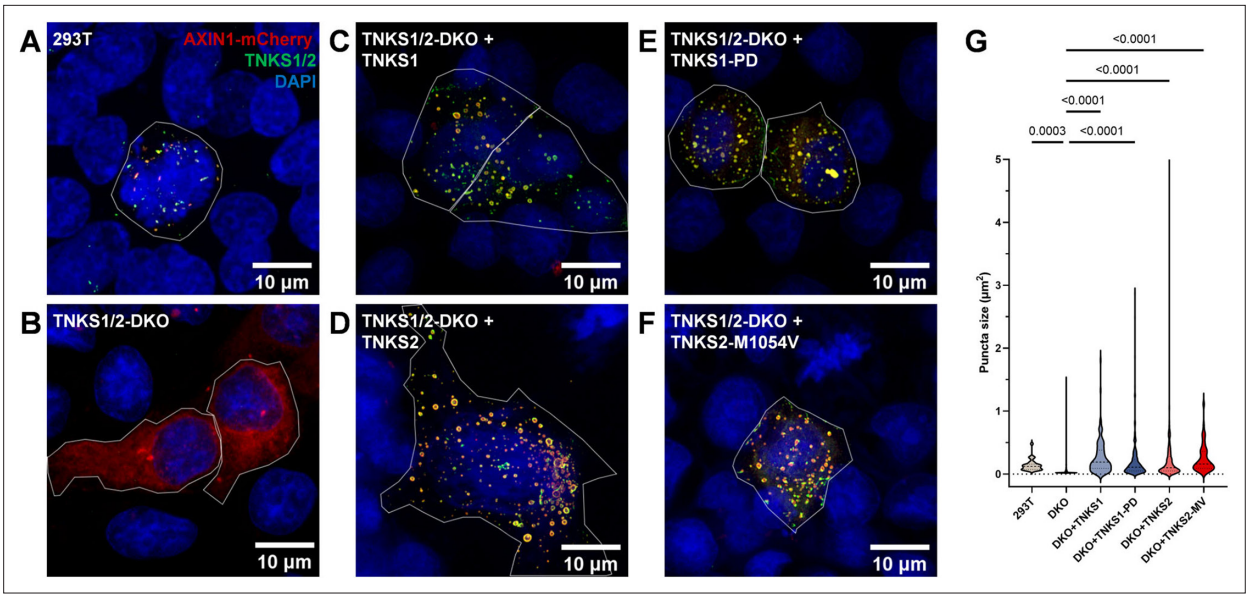


Figure 3. TNKS is required for AXIN puncta formation. (**A**) AXIN colocalized with TNKS and formed puncta in 293T cells transfected with AXIN1-mCherry plasmid. (**B**) AXIN distributed diffusely throughout the cytoplasm in TNKS1/2-DKO cells transfected with AXIN1-mCherry plasmid. (**C**) Introduction of TNKS1 restored AXIN puncta in TNKS1/2-DKO cells transfected with AXIN1-mCherry and TNKS1 plasmids. (**D**) TNKS2 also induced puncta formation in TNKS1/2-DKO cells transfected with AXIN1-mCherry and TNKS2 plasmids. (**E**) The catalytic function of TNKS1 is not required for puncta formation as demonstrated in TNKS1/2-DKO cells transfected with AXIN1-mCherry and TNKS1-PD plasmids. (**F**) Catalytically inactive TNKS2-M1054V also promoted AXIN puncta formation effectively in TNKS1/2-DKO cells transfected with AXIN1-mCherry and TNKS2-M1054V plasmids. (**G**) Quantification of the AXIN1-mCherry puncta in 293T cells (n=28 biological samples), TNKS1/2-DKO cells (n=230 biological samples), TNKS1/2-DKO cells in the presence of TNKS1 (n=115 biological samples), TNKS1/2-DKO cells in the presence of TNKS2 (n=229 biological samples), TNKS1/2-DKO cells in the presence of TNKS1-PD (n=246 biological samples), and TNKS1/2-DKO cells in the presence of TNKS2-M1054V (n=86 biological samples). Data are presented with p-values calculated by two-tailed unpaired *t*-test.

The online version of this article includes the following figure supplement(s) for figure 3:

Figure supplement 1. Effects of TNKS on AXIN puncta.

inactive variants of TNKS and found that both TNKS1-PD and TNKS2-M1054V could induce AXIN puncta effectively (***Figure 3E and F***). Quantitative imaging analysis confirmed that TNKS1 and TNKS2 promoted AXIN puncta formation through molecular scaffolding independently of their ability to catalyze protein PARylation (***Figure 3G***).

Both IWR1 and IWR1-POMA stabilize AXIN to suppress WNT/β-catenin signaling. However, IWR1 induces TNKS accumulation while IWR1-POMA promotes TNKS degradation. Given the observation that AXIN puncta formation requires TNKS, we next examined how these TNKS modulators affect the assembly of the DC. As expected, treating SW480 cells with IWR1 induced AXIN puncta while IWR1-POMA did not (***Figure 4A and B***). Similarly, IWR1 induced AXIN puncta in 293T cells wherein the endogenous AXIN1 was labeled with RFP at its C-terminus by CRISPR (***Kan et al., 2020***), but IWR1-POMA failed to induce AXIN puncta (***Figure 4C and D***). As 293T cells harbor wild-type APC and SW480 cells carry a truncating APC without the AXIN-binding sites (***Behrens et al., 1998***; ***Spink et al., 2000***), the ability of TNKSi to induce AXIN puncta is independent of AXIN-APC binding. These results also suggest that tagging AXIN1 with a fluorescent protein does not affect its ability to oligomerize.

To further understand the functional significance of AXIN puncta, we transfected HeLa cells with a low dose of AXIN1-GFP plasmid. Again, IWR1 promoted the formation of micrometer-sized AXIN puncta that are significantly larger than those observed in the DMSO control sample (***Figure 4E and F***). In contrast, AXIN1 distributed diffusely throughout the cytoplasm when the cells were treated with IWR1-POMA. To determine the effects of AXIN puncta on WNT signaling, we expressed AXIN1-GFP together with STF in HeLa cells under the same conditions and found that IWR1-POMA suppressed the luciferase activity better than IWR1 (***Figure 4G***). Thus, AXIN puncta formation is not a prerequisite for the DC to catalyze β-catenin degradation as commonly believed. Instead, the large AXIN puncta induced by IWR1 are less functional DCs than the unaggregated AXIN complexes formed

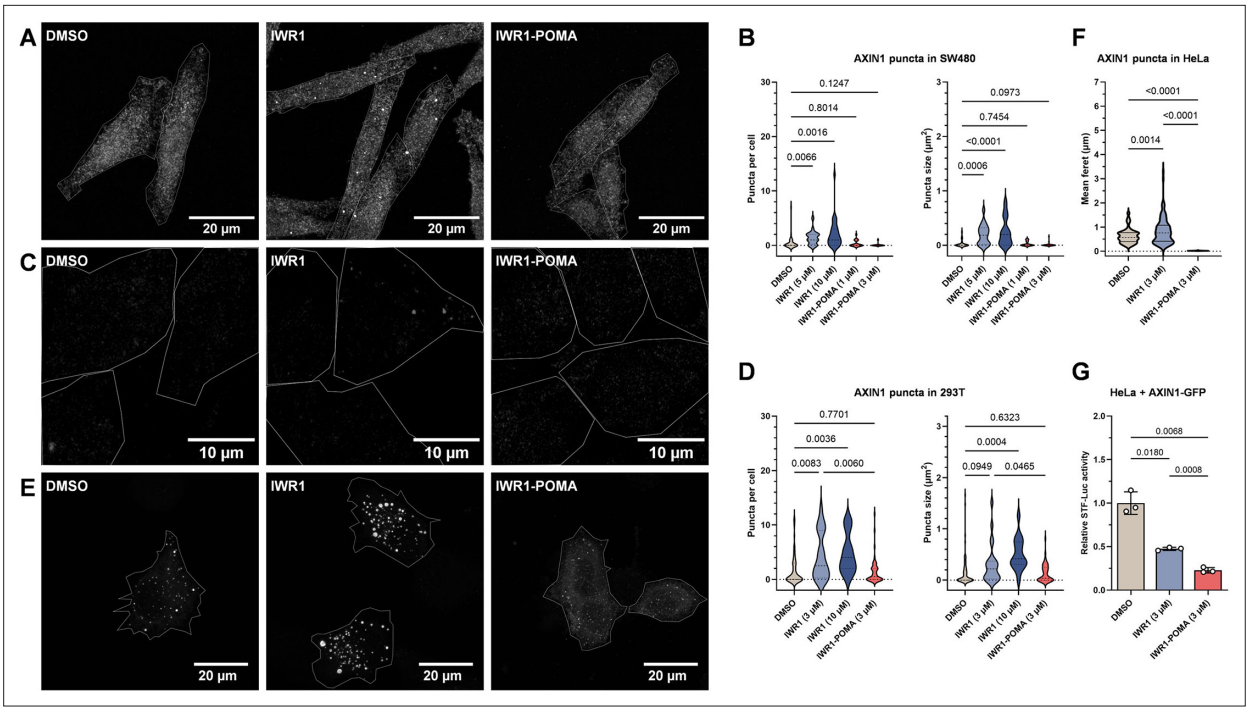


Figure 4. Chemically induced TNKS accumulation promoted AXIN puncta formation. (**A**) SW480 cells treated with DMSO, IWR1 (5 μM), or IWR1-POMA (1 μM) and stained with anti-AXIN1 antibody. (**B**) Numbers and sizes of the AXIN puncta in SW480 cells treated with DMSO (n=36 biological samples), IWR1 (5 μM, n=20 biological samples, or 10 μM, n=31 biological samples), or IWR1-POMA (1 μM, n=17 biological samples, or 3 μM, n=24 biological samples) for 16 h. (**C**) 293T-AXIN1-dsRed-KI cells treated with DMSO, IWR1 (3 μM), or IWR1-POMA (3 μM). (**D**) Numbers and sizes of the AXIN puncta in 293T-AXIN1-dsRed-KI cells treated with DMSO (n=82 biological samples), IWR1 (3 μM, n=39 biological samples, or 10 μM, n=32 biological samples), or IWR1-POMA (3 μM, n=61 biological samples) for 16 h. (**E**) HeLa cells were transfected with AXIN1-GFP plasmid and then treated with DMSO, IWR1 (3 μM), or IWR1-POMA (3 μM). IWR1 promoted the formation of micrometer-sized AXIN puncta whereas IWR1-POMA dissolved them. (**F**) Numbers and sizes of the AXIN1 puncta in HeLa cells transfected with AXIN1-GFP plasmid and treated with DMSO (n=88 biological samples), IWR1 (3 μM, n=91 biological samples), or IWR1-POMA (3 μM, n=151 biological samples) for 16 h. (**G**) HeLa cells transfected with AXIN1-GFP and STF plasmids and then treated with DMSO, IWR1 (3 μM) or IWR1-POMA (3 μM). IWR1-POMA suppressed WNT/β-catenin signaling significantly better than IWR1, indicating that AXIN puncta formation is not required for the DC to promote β-catenin degradation. Data are presented as mean ± SEM (n=3 biological samples) with p-values calculated by two-tailed unpaired *t*-test for all data.

The online version of this article includes the following figure supplement(s) for figure 4:

Figure supplement 1. TNKSi induced the formation of AXIN puncta.

upon IWR1-POMA treatment. We have further confirmed that the N-terminally tagged AXIN1 and the C-terminally tagged AXIN2 also responded to IWR1 and IWR1-POMA treatments in the same manner (***Figure 4—figure supplement 1C and D***).

The DC has been proposed to exist as biomolecular condensates (***Schaefer and Peifer, 2019***; ***Bienz, 2020***). Consistently, AXIN1-GFP formed puncta that exhibited fusion behavior in U2OS cells (***Figure 5—figure supplement 1***), supporting the notion that the DC possesses liquid-like properties, at least in the presence of excess AXIN1. TNKS interacts with both AXIN and APC and can self-aggregate to form insoluble filaments (***Thorvaldsen et al., 2015***; ***Sbodio et al., 2002***; ***Riccio et al., 2016***; ***De Rycker and Price, 2004***; ***Pillay et al., 2022***). We suspected that the massive accumulation of TNKS induced by IWR1 rigidified the DC (***Shin and Brangwynne, 2017***; ***Banani et al., 2017***) and limited its ability to turn over β-catenin. To test this hypothesis, we expressed AXIN1-mCherry and mNeonGreen-β-catenin in HeLa cells and then treated these cells with DMSO, IWR1 or IWR1-POMA. AXIN1-mCherry and mNeonGreen-β-catenin colocalized in all samples, indicating that labeling AXIN1 and β-catenin with a fluorescent protein did not disrupt the recruitment of β-catenin to the DC (***Figure 5A***). We then performed fluorescence recovery after photobleaching (FRAP) analysis on AXIN1-mCherry to investigate the structural role of TNKS in the DC. After photobleaching, the fluorescence signals of the AXIN-mCherry puncta in the DMSO control samples recovered quickly (k=0.093 s^{-1}, n=21), indicating a dynamic assembly of the DC (***Figure 5B***; ***Schwarz-Romond et al.,***

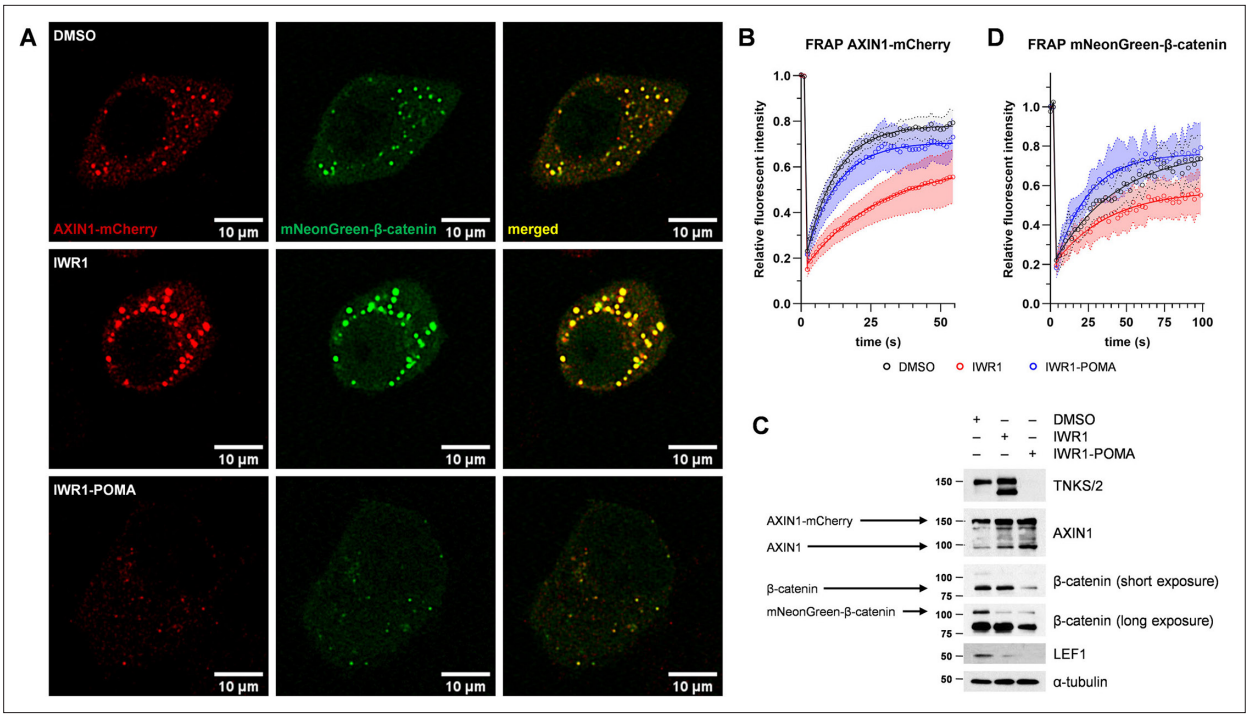


Figure 5. TNKS accumulation impeded the degradation of β-catenin. (**A**) HeLa cells were transfected with AXIN1-mCherry and mNeonGreen-β-catenin plasmids and then treated with DMSO, IWR1 (3 μM), or IWR1-POMA (3 μM). IWR1 promoted large AXIN1 puncta formation, and IWR1-POMA dissolved the puncta. β-Catenin colocalized with AXIN1, indicating the proper assembly of the DC. (**B**) FRAP analysis provided support to the hypothesis that TNKS controls the dynamic assembly of the DCs. IWR1 treatment led to a slow recovery of the AXIN1-mCherry fluorescent signal after photobleaching. In contrast, IWR1-POMA treatment did not affect the mobility of AXIN1. The fluorescent recovery curves were fitted to a one-phase association model. Data are presented as mean with 95% CI. (**C**) Western blot analysis of samples corresponding to (**A**) confirmed the accumulation of TNKS by IWR1 and the depletion of TNKS by IWR1-POMA. The deeper suppression of the Wnt/β-catenin signaling by IWR1-POMA is also supported by the reduced levels of total β-catenin. (**D**) FRAP analysis indicated that IWR1 limited the turnover of β-catenin. In contrast, IWR1-POMA accelerated the diffusion rate of β-catenin in the DC. The fluorescent recovery curves were fitted to a one-phase association model. Data are presented as mean with 95% CI.

The online version of this article includes the following source data and figure supplement(s) for figure 5:

Source data 1. PDF file for western blot analysis displayed in ***Figure 5D***.

Source data 2. Original files for western blot analysis displayed in ***Figure 5D***.

Figure supplement 1. Time-lapse imaging supports the liquid-like properties of AXIN puncta.

2007b; ***Nong et al., 2021***). However, the fluorescence signals of the AXIN1-mCherry puncta in the IWR1-treated sample recovered slowly (k=0.036 s^{-1}, n=16) and plateaued at 62% level, in contrast to 78% for the DMSO control, suggesting that IWR1 rigidified the DC. In contrast, the dynamics of the fluorescence recovery of the few very small AXIN1-mCherry puncta in the IWR1-POMA-treated sample was comparable to that of the DMSO control (k=0.090 s^{-1}, 71% recovery, n=21). Because both IWR1 and IWR1-POMA stabilized AXIN (***Figure 5C***), the rigidification of the DC by IWR1 is not a result of AXIN accumulation. Instead, as the DC puncta in the IWR1-treated sample was enriched with and that in the IWR1-POMA-treated sample depleted with TNKS, the reduction of the DC dynamics by IWR1 most likely originated from TNKS accumulation. We next performed FRAP analysis on mNeonGreen-β-catenin to examine the functional role of TNKS scaffolding in the DC using the dynamics of β-catenin as a measurement for its turnover rate (k=0.024 s^{-1}, 78% recovery, n=11 for the DMSO control). In contrast to IWR1-POMA that accelerated the fluorescence recovery of mNeonGreen-β-catenin (k=0.046 s^{-1}, 76% recovery, n=10), IWR1 reduced the level of recovery by 20% without affecting the kinetics (k=0.028 s^{-1}, 58% recovery, n=16). These results suggest that TNKSi functions in part through cytosolic retention of β-catenin, and TNKS accumulation negatively impacts the exchange of β-catenin in the DC (***Figure 5D***). Collectively, our data support the hypothesis that TNKS scaffolding augments AXIN puncta to limit the ability of the DC to effectively degrade β-catenin.

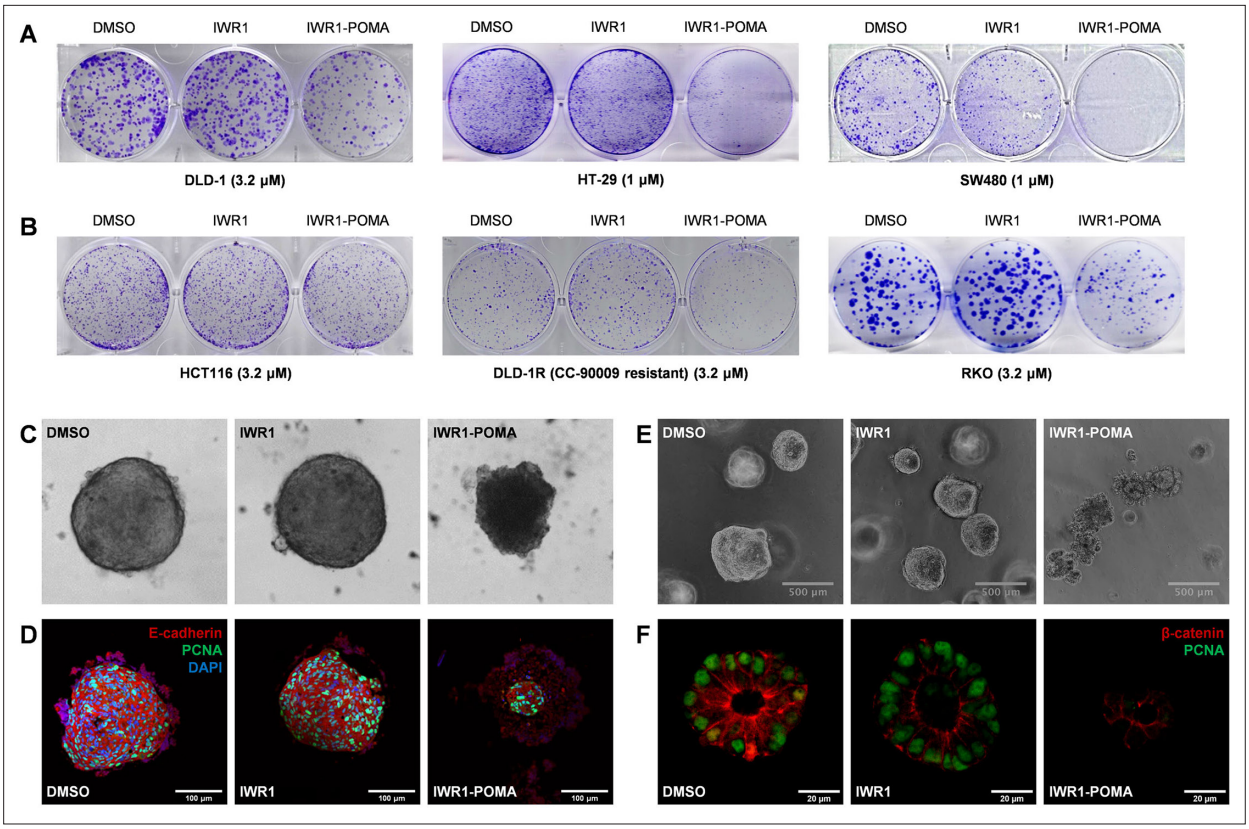


Figure 6. IWR1-POMA suppressed CRC cell growth. (**A**) IWR1-POMA suppressed the formation of DLD-1, SW480, and HT-29 CRC colonies significantly more effectively than IWR1. (**B**) HCT116 cells carrying a mutation in β-catenin that could not be processed by the DC were resistant to both IWR1 and IWR1-POMA. Additionally, DLD-1R cells obtained from cultivating DLD-1 cells with the GSPT1/2 inhibitor CC-90009 were still sensitive to IWR1-POMA treatment. IWR1-POMA could also inhibit RKO cells carrying full-length APC through the PTEN-AKT axis. (**C**) DLD-1 cells were developed into 3D spheroids and then treated with DMSO, IWR1 (5 μM), or IWR1-POMA (5 μM) for 10 days. The spheroids treated with IWR1-POMA lost the tight, spherical structure while IWR1 had no effect. (**D**) Immunostaining showed that the DLD-1 spheroids treated with IWR1-POMA only contained a small core of living cells while those treated with IWR1 remained highly proliferative. (**E**) IWR1-POMA (1 μM) suppressed the growth of PDM-7 patient-derived CRC organoids of approximately 200 μm in diameter with an apoptotic phenotype while IWR1 (1 μM) had no effect. (**F**) IWR1-POMA (1 μM) reduced the level of β-catenin and suppressed the proliferation of PDM-7 organoids grown from single cells significantly more effectively than IWR1 (1 μM).

The online version of this article includes the following source data and figure supplement(s) for figure 6:

Figure supplement 1. IWR1-POMA suppressed CRC growth through WNT inhibition.

Figure supplement 1—source data 1. PDF files for western blot analysis displayed in ***Figure 6—figure supplement 1D***.

Figure supplement 1—source data 2. Original files for western blot analysis displayed in ***Figure 6—figure supplement 1D***.

Figure supplement 2. IWR1-POMA suppressed CRC proliferation through on-target WNT inhibition.

Figure supplement 2—source data 1. PDF files for western blot analysis displayed in ***Figure 6—figure supplement 2***.

Figure supplement 2—source data 2. Original files for western blot analysis displayed in ***Figure 6—figure supplement 2***.

Figure supplement 3. IWR1-POMA demonstrated efficacy in CRC spheroid and primary organoid models.

Tankyrase degradation prevents CRC cell proliferation

Loss of functional APC impairs the DC function and results in constitutive WNT/β-catenin signaling that drives tumorigenesis and metastasis of CRC. Whereas depletion of both TNKS1 and TNKS2 by shRNA phenocopied APC restoration to prevent tumorigenesis in mice (***Schatoff et al., 2019***; ***Dow et al., 2015***), TNKSi only showed modest anti-proliferative activities in a limited number of CRC cell lines (***Mygland et al., 2021***). For example, IWR1 had minimal effects on the proliferation of DLD-1 cells that express truncated forms of APC. Remarkably, IWR1-POMA was able to suppress the formation of DLD-1 cell colonies under both normal and low serum conditions (***Figure 6A***, ***Figure 6—figure supplement 1A***). Similarly, the proliferation of SW480 and HT-29 cells carrying different truncating APC mutations was also better suppressed by IWR1-POMA (***Figure 6A***, ***Figure 6—figure supplement***

1B). The anti-proliferative activity also correlated with the ability of IWR1-POMA to better suppress WNT/β-catenin signaling in DLD-1 and SW480 cells (***Figure 6—figure supplement 1C***). Mechanistically, several WNT-controlled genes showed differential responses to IWR1 and IWR1-POMA. For example, whereas LEF1 was downregulated in both IWR1 and IWR1-POMA treated samples, cyclin D1 and Aurora kinase A responded to IWR1-POMA only in DLD-1 cells (***Figure 1F and G***, ***Figure 1—figure supplement 1D***). This observation is consistent with the ability of IWR1-POMA to better inhibit WNT/β-catenin signaling. Interestingly, IWR1-POMA also reduced the level of CDK4 while IWR1 had no effect, which may be explained by CDK4 being a direct target of c-MYC that in turn is a direct target of WNT/β-catenin. Indeed, IWR1-POMA reduced the level of c-MYC while IWR1 did not (***Figure 6—figure supplement 1D***). Taken together, targeted degradation of TNKS offers better control of the WNT/β-catenin pathway activities important to the maintenance of CRC cells than catalytic inhibition.

GSPT1, a translation termination factor that binds eRF1 to mediate translation termination, is frequently identified as a neosubstrate of CRBN in the presence of the IMiD class of small molecules (***Matyskiela et al., 2016***). For example, targeting GSPT1 for degradation by CC-90009 (eragidomide) perturbs the global proteome, activates the integrated stress response (ISR), and induces apoptosis in acute leukemia (AML) cells (***Baradaran-Heravi et al., 2021***; ***Sellar et al., 2022***). However, the observation that the VHL-based PROTACs could also induce TNKS1 degradation (***Figure 1—figure supplement 2C***) and the addition of IWR1 readily abolished the ability of IWR1-POMA to degrade TNKS (***Figure 1—figure supplement 3C***) suggest that IWR1-POMA did not deplete TNKS through affecting translation termination globally. Several lines of evidence further support that the observed growth inhibition by IWR1-POMA is a result of on-target degradation of TNKS. First, HCT116 cells harboring a mutation in one β-catenin allele that cannot be phosphorylated by the DC showed remarkable resistance to IWR1-POMA (***Figure 6B***, ***Figure 6—figure supplement 2A***). Second, IWR1-POMA had no effect on the level of cytosolic β-catenin in 293T-TNKS1/2-DKO cells that lack both TNKS1 and TNKS2 (***Figure 6—figure supplement 2B***), indicating that IWR1-POMA downregulated β-catenin in a TNKS-dependent manner. Third, the GSPT1/2 degrader CC-90009 had no effect on TNKS and the cytosolic β-catenin levels in DLD-1 cells (***Figure 6—figure supplement 2C***). Fourth, we have further exposed DLD-1 cells to CC-90009 and established resistant cells (DLD-1R) that lacked the expression of GSPT1/2 (***Figure 6—figure supplement 2D***). TNKS in DLD-1R remained responsive to IWR1 and IWR1-POMA treatments (***Figure 6—figure supplement 2E***), and IWR1-POMA was still able to prevent the proliferation of DLD-1R cells effectively (***Figure 6B***, ***Figure 6—figure supplement 2F***). As such, IWR1-POMA suppressed WNT-dependent cancer cell proliferation through degrading TNKS but not GSPT1/2. However, consistent with catalytic inhibition or knocking down both TNKS1 and TNKS2 stabilized PTEN and suppressed the growth of RKO cells (***Li et al., 2015***), IWR1-POMA also suppressed the proliferation of RKO cells that carry full-length APC (***Figure 6B***, ***Figure 6—figure supplement 2G***). This result indicates that targeting TNKS by IWR1-POMA can also suppress cancer cell growth through the PTEN-AKT axis independently of the WNT/β-catenin pathway.

To investigate the anticancer potential of IWR1-POMA further, we used DLD-1 and SW480 cells to establish 3D spheroids that recapitulated the cell–cell interactions and the hypoxia core of tumors. Consistent with colony formation assays, IWR1 had no effect on the size and the morphology of these spheroids, while IWR1-POMA suppressed their growth effectively (***Figure 6C***, ***Figure 6—figure supplement 3A***). Notably, the outer layer of the spheroids treated by IWR1-POMA had a loose structure incapable of supporting a spherical shape. Instead, they adapted a rather flat architecture with a small core of aggregated cells. Immunostaining showed that the outer layer of these IWR1-POMA-treated spheroids did not contain living cells (***Figure 6D***). The presence of significant DNA breaks in this region (***Figure 6—figure supplement 3B***) is consistent with the observation that APC restoration induced apoptosis in CRC cells (***Morin et al., 1996***).

We have also evaluated the anticancer effects of IWR1-POMA in a human CRC organoid model that preserved the multicellular identity of the tumor more faithfully than immortalized cancer cells. The PDM-7 patient-derived primary CRC cells harbor truncating mutations in APC, making it susceptible to WNT inhibition. We first confirmed that the PDM-7 organoids maintained the heterogeneous nature of the proliferation and the WNT activity within the organoids (***Figure 6—figure supplement 3C***). We next confirmed that IWR1-POMA could prevent the formation of PDM-7 organoids, whereas IWR1 had little or no effect (***Figure 6—figure supplement 3D***). We then treated established PDM-7 organoids with IWR1 or IWR1-POMA and found that, in contrast to IWR1 that did not affect their

growth, IWR1-POMA inhibited the proliferation of these organoids with an apoptotic phenotype (***Figure 6E***, ***Figure 6—figure supplement 3E and F***) and promoted β-catenin degradation more effectively than IWR1 (***Figure 6D***). Collectively, removing TNKS scaffolding is important for achieving anticancer efficacy in CRC by targeting TNKS.

Discussion

In the existing model of WNT/β-catenin signaling, AXIN is a key component of the DC. It interacts with APC to work as a scaffolding protein for the DC to catalyze β-catenin phosphorylation and ubiquitination. In the cytoplasm, TNKS also associates with the DC and controls the AXIN level through PARdU (***Huang et al., 2009***; ***Zhang et al., 2011***; ***DaRosa et al., 2015***). As such, AXIN accumulates upon TNKS inhibition, leading to enhanced β-catenin degradation and reduced WNT/β-catenin pathway activities (***Huang et al., 2009***; ***Chen et al., 2009***). Traditionally, the formation of AXIN puncta is viewed as a hallmark of functional DC induction (***de la Roche et al., 2014***; ***Thorvaldsen et al., 2015***; ***Martino-Echarri et al., 2016***), wherein the increased local concentration of DC components enhances its 'effective activity' (***Schaefer et al., 2018***; ***Pronobis et al., 2015***). Because TNKS inhibition induces large AXIN puncta, it is generally believed that TNKSi supports the formation of highly functional DCs to accelerate the turnover of β-catenin. However, given the newly discovered role of TNKS scaffolding (***Mariotti et al., 2016***; ***Riccio et al., 2016***), the mechanism by which TNKS controls WNT signaling needs refinement. In this study, we show that AXIN puncta formation relies on the scaffolding but not the catalytic function of TNKS, which is consistent with the previous report that knocking down both TNKS1 and TNKS2 prevented G007-LK to induce AXIN puncta in SW480 cells (***Martino-Echarri et al., 2016***). However, the functional role of TNKS scaffolding in the DC remained unaddressed. Interestingly, blocking proteasomal degradation by MG132 promoted TNKS accumulation, but the resulting DC exhibited a different phenotype as compared to that induced by G007-LK (***Martino-Echarri et al., 2016***). It is likely that the PAR chains helped suppress TNKS aggregation as observed with PARP1.

The DC exhibits characteristics of biomolecular condensates (***Schaefer and Peifer, 2019***; ***Bienz, 2020***). It contains tens to hundreds of AXIN and APC molecules in an ~1:1 ratio to catalyze β-catenin degradation (***Schaefer et al., 2018***). Both AXIN and APC contain extensive intrinsically disordered regions, which are likely important for providing a flexible structure to support catalysis. TNKS interacts with AXIN and APC through multivalent binding in the DC. Based on this work, the catalysis-independent function of TNKS in WNT/β-catenin signaling originates from its ability to promote maturation (***Shin and Brangwynne, 2017***; ***Banani et al., 2017***) of the DC condensates. Specifically, because TNKS aggregates and forms filaments at high concentrations (***Sbodio et al., 2002***; ***De Rycker and Price, 2004***; ***Pillay et al., 2022***), large AXIN puncta containing excess TNKS are rigid and exhibit reduced catalytic activity. In contrast, in the absence of TNKS, the small AXIN complexes are dynamic and catalyze β-catenin degradation more effectively. As such, the size of the AXIN complex does not inform the activity of the DC. This notion is consistent with the previous observation that AXIN2 can also support β-catenin degradation despite having a reduced ability to form puncta (***Bernkopf et al., 2019***). Collectively, our study suggests that TNKS controls WNT/β-catenin signaling through two independent mechanisms: it regulates AXIN homeostasis through catalytic PARylation (***Huang et al., 2009***); meanwhile, it dictates the material properties of the DC through molecular scaffolding. The mechanism by which TNKS antagonizes the DC through molecular scaffolding is also reminiscent of the effect of disheveled (DVL) polymerization on the WNT/β-catenin signalosome (***Schwarz-Romond et al., 2007a***). However, characterization of the physical properties of reconstituted DC (***Ranes et al., 2021***) with TNKS is needed to better understand the nature of these condensates.

The development of TNKSi as an anticancer drug has been discouraged by the lack of significant efficacy in various in vitro and in vivo models. Our data suggest that TNKSd can overcome this limitation by stabilizing AXIN without affecting the DC dynamics. Therefore, TNKSd can provide better suppression of the WNT/β-catenin-controlled genes important for cancer cell proliferation than TNKSi. In particular, we identify several WNT target genes that are suppressed by TNKSd but not TNKSi. Among them, Aurora A is an oncogene frequently amplified in CRC (***Bischoff et al., 1998***). Because Aurora A binds to and stabilizes c-MYC that is also dysregulated in many cancers (***Dauch et al., 2016***), the ability of IWR1-POMA to downregulate both c-MYC and Aurora A more effectively than IWR1 likely contributed to its improved anti-proliferative activity. Another WNT/β-catenin downstream target specifically regulated by TNKSd is cyclin D1. The CDK4/cyclin D1 complex is a key

regulator of the cell cycle, and CDK4 blockade has been explored as a potential strategy to enhance the anticancer efficacy of TNKSi (**Menon et al., 2019**; **Foronda et al., 2019**). Interestingly, TNKSd, but not TNKSi, also downregulated CDK4 expression potentially through c-MYC. We speculate that the coordinated action of IWR1-POMA on CDK4 and cyclin D1 additionally contributed to its improved anticancer efficacy. Finally, TNKSi can sensitize cancer cells toward EGFR or MEK inhibition (**Wang et al., 2016**; **Schoumacher et al., 2014**). As a more effective suppressor of Wnt/β-catenin signaling, IWR1-POMA may provide a better therapeutic window for treating cancers driven by WNT/β-catenin signaling using a corresponding combinatorial approach.

Some previous studies showed that TNKSi induced reversible intestinal toxicity at high doses without significant antitumor effects in mice (**Lau et al., 2013**; **Zhong et al., 2016b**). However, others found that suppressing the proliferation of *Lgr5*$^{+}$ intestinal stem cells by TNKSi did not affect the morphology of the tissue or cause weight loss (**Norum et al., 2018**; **Zhong et al., 2016a**; **Tian et al., 2011**), and the selective TNKS inhibitor basroparib was well tolerated in a recently disclosed phase 1 clinical study (**Lieu et al., 2025**). As constitutive silencing of TNKS in *APC*-null mice prevented tumorigenesis without damaging the intestines (**Schatoff et al., 2019**), the observed on-target toxicity of TNKSi may associate with TNKS accumulation at high doses, akin to the cytotoxicity induced by PARP1-trapping upon catalytic inhibition, and reverse allostery (**Langelier et al., 2018**) in TNKS has been proposed (**Pillay et al., 2022**). Studying TNKS complexes in normal tissues under these conditions may help delineate the source of intestinal toxicity. Finally, targeting the TNKS ARC or SAM domains offers an alternative approach to suppress WNT/β-catenin signaling without promoting TNKS oligomerization (**Pollock et al., 2019**; **Sowa et al., 2020**). Targeting the ARC may further differentiate the WNT-dependent and independent activities of TNKS and provide finer resolution in TNKS inhibition. We are thus cautiously optimistic for continued investment in aggregation-free TNKS-targeting in CRC.

Materials and methods

Key resources table

Reagent type (species) or resource	Designation	Source or reference	Identifiers	Additional information
Cell line (*Homo sapiens*)	HAP1	Horizon Discovery	C631 (CVCL_Y019)	
Cell line (*Homo sapiens*)	DLD1	ATCC	CCL-221 (CVCL_0248)	
Cell line (*Homo sapiens*)	HCT 116	ATCC	CRL-247 (CVCL_0291)	
Cell line (*Homo sapiens*)	HEK293	ATCC	CRL-1573 (CVCL_0045)	
Cell line (*Homo sapiens*)	239T	ATCC	CRL-3216 (CVCL_0063)	
Cell line (*Homo sapiens*)	HeLa	ATCC	CCL-2 (CVCL_0030)	
Cell line (*Homo sapiens*)	HT-29	ATCC	HTB-38 (CVCL_0320)	
Cell line (*Homo sapiens*)	SW480	ATCC	CCL-228 (CVCL_0546)	
Cell line (*Homo sapiens*)	RKO	ATCC	CRL-2577 (CVCL_0504)	
Cell line (*Homo sapiens*)	U-2 OS	ATCC	HTB-96 (CVCL_0042)	
Cell line (*Homo sapiens*)	L-Wnt3A	ATCC	CRL-2647 (CVCL_0635)	
Cell line (*Homo sapiens*)	PDM-7	ATCC	HCM-CSHL-0063-C18	
Antibody	TNKS1/2 mouse monoclonal antibody (E-10)	Santa Cruz	sc-365897 (RRID:AB_10844977)	(1:1000)
Antibody	AXIN1 rabbit monoclonal antibody (C76H11)	Cell Signaling	#2087 (RRID:AB_2274550)	(1:1000)
Antibody	AXIN2 rabbit monoclonal antibody (76G6)	Cell Signaling	#2151 (RRID:AB_2062432)	(1:1000)
Antibody	β-catenin rabbit monoclonal antibody (D10A8)	Cell Signaling	#8480 (RRID:AB_11127855)	(1:1000)

Continued on next page

Continued

Reagent type (species) or resource	Designation	Source or reference	Identifiers	Additional information
Antibody	c-Myc rabbit monoclonal antibody (D84C12)	Cell Signaling	#5605 (RRID:AB_1903938)	(1:1000)
Antibody	Cyclin D1 rabbit monoclonal antibody (E3P5S)	Cell Signaling	#55506 (RRID:AB_2827374)	(1:1000)
Antibody	CDK4 rabbit monoclonal antibody (D9G3E)	Cell Signaling	#12790 (RRID:AB_2631166)	(1:1000)
Antibody	Aurora A rabbit monoclonal antibody (D3E4Q)	Cell Signaling	#14475 (RRID:AB_2665504)	(1:1000)
Antibody	LEF1 rabbit monoclonal antibody (C12A5)	Cell Signaling	#2230 (RRID:AB_823558)	(1:1000)
Antibody	GAPDH rabbit monoclonal antibody (D16H11)	Cell Signaling	#5174 (RRID:AB_10622025)	(1:1000)
Antibody	α-Tubulin mouse monoclonal antibody (AA13)	Sigma	T8203 (RRID:AB_1841230)	(1:1000)
Antibody	FLAG mouse monoclonal antibody (M2),	Sigma	F1804 (RRID:AB_262044)	(1:1000)
Antibody	Vinculin mouse monoclonal antibody (hVIN-1)	Sigma	V9264 (RRID:AB_10603627)	(1:1000)
Antibody	GSPT1 rabbit polyclonal antibody	Abcam	Ab126090 (RRID:AB_11128263)	(1:1000)
Antibody	GSPT2 rabbit polyclonal antibody	Invitrogen	PA5-60824 (RRID:AB_2642245)	(1:1000)
Biological sample	Collagen I, rat tail	Thermo Fisher	A1048301	
Commercial assay or kit	TMT10plex Isobaric Label Reagents and Kits	Thermo Fisher	#90110	
Commercial assay or kit	QUANTI-Luc Gold	Invivogen	rep-qlcg2	
Commercial assay or kit	Dual-Luciferase Reporter Assay System	Promega	E1960	
Commercial assay or kit	Organoid Growth Kit 1A	ATCC	ACS-7100	
Chemical compound, drug	Y-27632	ATCC	ACS-3030	
Chemical compound, drug	MG-132	Selleck	S2619	
Chemical compound, drug	Pomalidomide	Selleck	S1567	
Chemical compound, drug	Eragidomide (CC-90009)	Cayman	#33692	

Cell lines

The identities of all immortalized human cell lines were authenticated by the vendors prior to shipment and subsequently confirmed by STR profiling. HCT116 cells are MSI-high; genotyping confirmed a heterozygous CTNNB1 genotype, with one wild-type allele and one allele harboring the p.Ser45del (c.133_135delTCT) variant. HeLa is reported as a contaminating cell line in the ICLAC Register but itself is not a misidentified cell line. None of the other cell lines is listed in the ICLAC Register. All these cells were cultured according to the vendors' recommended procedures and routinely screened and confirmed negative for mycoplasma contamination. All experiments were performed using low-passage cells (passages 3–12) within 3 months of thawing. L-Wnt3A cells were used to generate conditioned medium following the protocol described by Nusse (https://wnt.stanford.edu/purification%23old#medium). PDM-7 obtained from ATCC were grown into organoid according to the procedures provided by ATCC using the Organoid Growth Kit 1A and cell basement membrane for organoid culture from ATCC.

CRISPR engineering of HAP1 cells

HAP1 cells were transiently transfected with pCRISPaint-NanoLuc-PuroR and pCAS9-mCherry-Frame+2 plasmids and a TNKS1 sgRNA plasmid targeting 5′-TCACTAGGTCTTCTGCTCTGCGG-3′ and selected by puromycin treatment. Cells were then cultured in 96 well plates to generate single colonies and sequenced to select for correct incorporation of nanoluciferase at the C-terminus of TNKS1.

DLD-1R cells

DLD-1 cells were cultivated with an increasing concentration of CC-90009 (0.1, 1, and 10 μM) to confer resistance to GSPT inhibition. Western analysis confirmed the loss of GSPT1 expression in these cells. GSPT2 is a low-abundance protein in DLD-1 and DLD-1R not detectable by western blot, which is consistent with a reported quantitative proteomic analysis of DLD-1 cells (GSPT1: 102,567 ppb, GSPT2: 2495 ppb; https://www.ebi.ac.uk/gxa/experiments/E-PROT-18/Results) (***Wang et al., 2017***).

Determination of TNKS degradation

HAP1-TNKS1-NanoLuc cells at 30–50% confluence were treated with different concentrations of PROTAC molecules in triplicates for 16 h. The TNKS1 level was quantified by QUANTI-Luc Gold (Invivogen) with normalization to the total protein content. For high-throughput screens, the cells were seeded into 96-well plates at 2×10^4 cells per well with 100 μL culture media. The PROTAC molecules dissolved in DMSO were placed in T8+ dispensehead cassettes and then introduced by the TECAN D300e Digital Dispenser with series dilutions under the D300e software control. To determine the DC_{50} value of IWR1-POMA, the dose–response relationship was fitted to a Bayesian Gaussian Processes model in R using code developed by Semenova (***Semenova et al., 2021***).

Immunoblot assays

Cells were washed once with cold PBS and lysed with the SDS lysis buffer (1% SDS, 10 mM HEPES, pH 7.0, 2 mM $MgCl_2$, and 500 U universal nuclease). Subcellular protein fractions were obtained by using the Mem-PER Plus Kit (Thermo Fisher Scientific). Briefly, the cell pellets were suspended in the cell permeabilization buffer with cOmplete EDTA-free protease inhibitor cocktail (Sigma) and incubated for 15 min at 4°C followed by centrifugation at 16,000×*g* for 15 min to provide the cytosolic fraction. The pellets were then suspended in the cell permeabilization buffer with 0.5% NP-40 and protease inhibitors, passed through a 27½-gauge needle for 30 times, and centrifuged at 16,000×*g* for 15 min to give the cytosolic fraction, and the pellets were suspended in RIPA buffer with protease inhibitors with sonication to provide the nuclear fraction. Alternatively, cells were incubated in eight volumes of hypotonic buffer (20 mM HEPES-KOH, pH 7.9; 10 mM KCl; 2 mM $MgCl_2$; 0.3% NP-40; 1 mM DTT; 1 mM EDTA; and 1× protease inhibitor cocktail) on ice for 20 min and then centrifuged at 3000×*g* for 10 min at 4°C to provide the cytosolic extracts. Protein concentrations were determined by the BCA assay kit (Thermo Fisher Scientific). A total of 20 μg of proteins were loaded onto the SDS–PAGE gel and then transferred to a nitrocellulose membrane. Nitrocellulose membranes were then blocked with Tris buffered saline containing 0.1% Tween-20 and 5% milk (Bio-Rad). Membranes were incubated with the primary antibodies overnight at 4°C and then the secondary antibodies for 1 h at room temperature. The blots were developed with or without enhanced chemiluminescence and were exposed on autoradiograph films or imaged using a Bio-Rad Molecular Imager ChemiDoc XRS System.

Quantitative mass spectrometry

DLD-1 cells at 40% confluence were treated with the drug for 24 h, washed with cold PBS, and lysed with the SDS lysis buffer. Protein concentrations were determined by the BCA assay kit (Thermo Fisher Scientific). Two biological replicate samples were prepared with 500 μg of proteins from each sample, reduced with 2 mM DTT for 10 min, and alkylated with 50 mM iodoacetamide for 30 min in the dark, and then extracted using methanol-chloroform precipitation. The protein pellets were dissolved in 400 μL 8 M urea buffer (8 M urea, 50 mM Tris-HCl, 10 mM EDTA, pH 7.5) and digested by Lys-C (Wako, at a 1:100 enzyme/protein ratio) for 2 h. The urea concentration was then reduced to 2 M using freshly made 100 mM ammonium bicarbonate solution. Proteins were subsequently digested with trypsin (Thermo Fisher Scientific, at 1:100 enzyme/protein ratio) overnight. Peptides were desalted with Oasis HLB cartridges (Waters) and re-suspended in 200 mM HEPES (pH 8.5) to a final concentration of 1 μg/

μL. For each sample, 100 μg of peptides were reacted with the corresponding amine-based TMT reagents (Thermo Fisher Scientific) for 1 h. The reactions were quenched with 5% hydroxylamine solution and were combined. Samples were then desalted and a reverse-phase fractionation spin column (Pierce) was used according to the manufacturer's directions to fractionate the sample into eight fractions. The fractions were dried in a SpeedVac and reconstituted in a 2% acetonitrile, 0.1% TFA buffer followed by injecting onto an Orbitrap Fusion Lumos mass spectrometer coupled to an Ultimate 3000 RSLC-Nano liquid chromatography system. Samples were injected onto a 75 μm×75 cm EasySpray column (Thermo) and eluted with a gradient from 0→28% buffer B over 180 min. Buffer A contained 2% (v/v) acetonitrile and 0.1% formic acid in water, and buffer B contained 80% (v/v) acetonitrile, 10% (v/v) trifluoroethanol, and 0.1% formic acid in water. The mass spectrometer operated in positive ion mode with a source voltage of 1.8 kV and an ion transfer tube temperature of 275°C. MS scans were acquired at 120,000 resolution in the Orbitrap and top speed mode was used for SPS-MS3 analysis with a cycle time of 2.5 s. MS2 was performed with CID with a collision energy of 35%. The top 10 fragments were selected for MS3 fragmentation using HCD, with a collision energy of 55%. Dynamic exclusion was set for 25 s after an ion was selected for fragmentation. The raw MS data files were analyzed using Proteome Discoverer v2.4 (Thermo), with peptide identification performed using Sequest HT searching against the human protein database from UniProt. Fragment and precursor tolerances of 10 ppm and 0.6 Da were specified, and three missed cleavages were allowed. Carbamidomethylation of Cys and TMT10plex labeling of N-termini and Lys side-chains were set as fixed modifications, with oxidation of Met set as a variable modification. Protein abundances were determined based on the sum of the signal-to-noise ratios of the reporter ions for all peptides matched to each protein. The false discovery rate (FDR) cutoff was 1% for all peptides. Statistical analyses (one-way ANOVA and two-sided unpaired *t*-tests) were performed in R using the peptide data. The MS data have been deposited in the MassIVE repository with the dataset identifier MSV000089098.

Luciferase reporter assays

L-Wnt3A-STF cells, or HeLa, DLD-1, or SW480 cells expressing STF and Renilla-luciferase at 30–50% confluence were treated with the indicated compound for 16 h. The STF-firefly and Renilla luciferase activities were measured using the Dual Luciferase kit (Promega). The WNT/β-catenin pathway activities were determined by normalizing the STF-firefly activity to the Renilla activity or the total protein level. Briefly, cells were transfected with or without STF plasmid (Addgene) and pRL Renilla luciferase plasmid (Addgene) using Lipofectamine 3000 (Thermo Fisher Scientific) in Opti-MEM for 5 h and empty cloning vector as negative control. After incubating in cell growth media for 3 h, cells were collected and reseeded into 24- or 96-well plates. After incubating for 4 h, cells were treated with the indicated small molecules for 16–24 h and then washed with PBS, and then lysed with Passive Lysis Buffer (Promega) before luciferase activity was measured according to the manufacturer's instructions. Statistical analyses (one-way ANOVA and two-sided unpaired *t*-tests) were performed in GraphPad Prism.

BRET analysis

HAP1-TNKS1-NanoLuc cells (2×10^4 cells) treated with MG132 (1 μM) for 2 h or 293T cells (1×10^4 cells) transfected with TNKS1-NanoLuc plasmid (25 ng) for 24 h were treated with different concentrations of IWR1 in the presence of IWR1-POMA (0.5 μM) or IWR1-PEG3-NCT (0.5 μM) for 2 h in Opti-MEM without phenol red in 96-well plates. NanoBRET NanoGlo Substrate (Promega) was then added and the fluorescence signals were measured at 450 and 610 nm on a BioTek Synergy Neo2 microplate reader. The BRET signals were determined as the 610 nm (acceptor) emission over 450 nm (donor) emission ratio after background correction.

Immunofluorescence microscopy

HeLa cells at 30–50% confluence in a 35 mm dish were transfected with 30 ng of the indicated plasmids for 6 h and then treated with DMSO, IWR (3 μM), or IWR1-POMA (3 μM) for 16 h. Images were obtained using a Zeiss LSM 880 Airyscan confocal laser scanning microscope. FRAP analysis was performed at room temperature in the DMEM media without phenol red and with HEPES supplement and the indicated drugs. Defined regions were photobleached at a specific wavelength using the 405 nm or 561 nm laser, and the fluorescence intensities in these regions were collected every 2 s and

normalized to the initial intensity before bleaching. The fluorescent signal intensities were determined in ImageJ and analyzed in GraphPad Prism.

2D colony formation assays

DLD-1, SW480, HT-29, HCT116, RKO, or DLD-1R cells were seeded into 6-well plates at 500–2000 cells/well with 10% FBS unless otherwise mentioned in the growth medium. Compounds were added at the indicated concentrations 16 h after seeding, and the growth medium was replenished every 3 days until colony formation was observed. The colonies were fixed with 4% formalin in PBS and stained by a solution of 0.5% crystal violet in 50% methanol solution.

3D spheroid formation assay

DLD-1 or SW480 cells were seeded at 1000 cells/well into 96-well plates with 10% FBS in the Hyclone X growth medium. For DLD-1 cells, 3D spheroids formed 1 day after seeding. For SW480 cells, rat tail collagen I was added to provide the extracellular matrix, and 3D spheroids formed 5 days after seeding. Compounds were then added at the indicated concentrations. Medium with the indicated drug was replenished every 3 days, and the size of the spheroids was measured at the indicated time by imaging on a Cytation 5 Cell Imaging Multimode Reader and analyzed using ImageJ. The spheroids at the endpoints were fixed with 4% formalin in PBS, sectioned, and stained with the indicated markers after parafilm embedding.

CRC organoid formation assay

The organoids were cultured according to the procedures detailed by ATCC. Briefly, dissociated PDM-7 single cells or organoid fragments of about 200 μM diameter in size were embedded at 5,000,000 cells/mL in the cell base membrane and dispensed as small droplets onto warm 6-well plates. After solidification, the domes were covered with the advanced DMEM:F12 supplemented with HEPES, L-glutamine and B-27, noggin, gastrin, N-acetyl-cysteine, EGF, nicotinamide, A 83-01, and SB 202190 (ATCC formulation 1). The ROCK inhibitor Y-27632 (10 μM) was also included for the first 3 days of subculture. The organoids were treated with the drug 3 days after seeding for 5 days in the single-cell model and 1 day after seeding for 5 days in the organoid fragment model.

Synthetic procedures

Synthesis of IWR1-TP4-Poma (IWR1-POMA)

To a solution of [*1127442-97-0*] (***Chen et al., 2009***) (351 mg, 0.8 mmol, 1.0 equiv) in methylene chloride (3 mL) was added methanesulfonyl chloride (183 mg, 1.6 mmol, 2.0 equiv), triethylamine (0.33 mL, 2.4 mmol, 3.0 equiv) at 0°C. After stirring for 2 h, the reaction mixture was concentrated, the residual was re-dissolved in *N*,*N*-dimethylformamide (3 mL), and sodium azide (208 mg, 3.2 mmol, 4.0 equiv) was then added. After stirring at 50°C overnight, the reaction was quenched with water and extracted with ethyl acetate three times. The combined organic layers were washed with brine, dried over sodium sulfate, concentrated, and purified by silica gel flash column chromatography to give azido-IWR2 (335 mg, 90% yield) as a white powder. ^{1}H NMR (400 MHz, $CDCl_3$) δ 10.74 (s, 1H), 8.90 (dd, *J*=6.0, 3.0 Hz, 1H), 8.78 (d, *J*=4.4 Hz, 1H), 8.09 (d, *J*=8.1 Hz, 2H), 7.63–7.56 (m, 2H), 7.47 (d, *J*=4.4 Hz, 1H), 7.36 (d, *J*=8.2 Hz, 2H), 6.28 (t, *J*=1.8 Hz, 2H), 4.82 (s, 2H), 3.54–3.50 (m, 2H), 3.46 (dd, *J*=3.1, 1.6 Hz, 2H), 1.79 (d, *J*=8.6 Hz, 1H), 1.62 (d, *J*=8.8 Hz, 1H); MS (ESI) calcd for $C_{26}H_{21}N_6O_3$ $(M+H)^+$ 465.2, found 465.2.

To a solution of azido-IWR2 (4.2 mg, 0.009 mmol, 1.0 equiv) in dimethyl sulfoxide was added [*2138439-58-2*] (***Steinebach et al., 2019***) (5 mg, 0.01 mmol, 1.1 equiv), copper(II) sulfate pentahydrate (4.5 mg, 0.018 mmol, 2.0 equiv), and (+)-sodium l-ascorbate (7.2 mg, 0.036 mmol, 4.0 equiv). After stirring at 80°C overnight, the reaction was quenched with saturated ammonium chloride and extracted with methylene chloride three times. The combined organic layers were washed with brine, dried over sodium sulfate, concentrated, and purified by silica gel flash column chromatography followed by preparative HPLC to give IWR1-TP4-Poma (IWR1-POMA) (5.4 mg, 63% yield) as a yellow solid. ^{1}H NMR (400 MHz, $CDCl_3$) δ 10.75 (s, 1H), 8.94 (dd, *J*=7.0, 1.9 Hz, 1H), 8.77 (d, *J*=4.4 Hz, 1H), 8.38 (s, 1H), 8.14–8.07 (m, 2H), 7.73–7.58 (m, 3H), 7.44 (dd, *J*=8.5, 7.1 Hz, 1H), 7.40–7.34 (m, 2H), 7.07 (dd, *J*=7.9, 5.7 Hz, 2H), 6.85 (d, *J*=8.5 Hz, 1H), 6.29 (t, *J*=1.9 Hz, 2H), 6.02 (s, 2H), 4.87 (dd, *J*=12.0, 5.4 Hz, 1H), 4.70 (s, 2H), 3.74–3.58 (m, 14H), 3.54 (dq, *J*=3.5, 1.7 Hz, 2H), 3.49 (dd, *J*=3.0, 1.6 Hz, 2H), 3.41

(t, *J*=5.3 Hz, 2H), 2.89–2.66 (m, 3H), 2.14–2.04 (m, 1H), 1.82 (dt, *J*=8.9, 1.7 Hz, 1H), 1.65 (d, *J*=8.9 Hz, 1H); MS (ESI) calcd for $C_{50}H_{50}N_9O_{11}$ $(M+H)^+$ 952.4, found 952.3.

Synthesis of IWR1-TP(n)-Poma

Prepared using the same method as described for IWR1-TP4-Poma using pomalidomide derivatives with different PEG chain lengths.

IWR1-TP1-Poma

7.4 mg, 41% yield. ^{1}H NMR (400 MHz, $CDCl_3$) δ 10.73 (s, 1H), 8.95 (dd, *J*=6.3, 2.7 Hz, 1H), 8.74 (d, *J*=4.3 Hz, 1H), 8.12 (dt, *J*=9.1, 1.8 Hz, 3H), 7.71–7.61 (m, 3H), 7.44 (ddd, *J*=8.4, 7.0, 1.1 Hz, 1H), 7.40–7.36 (m, 2H), 7.07 (d, *J*=7.1 Hz, 1H), 7.01 (d, *J*=4.5 Hz, 1H), 6.86 (d, *J*=8.5 Hz, 1H), 6.29 (q, *J*=1.6 Hz, 2H), 6.03 (s, 2H), 4.84 (dd, *J*=12.0, 5.4 Hz, 1H), 4.71 (s, 2H), 3.74 (d, *J*=5.3 Hz, 2H), 3.54 (dq, *J*=3.3, 1.6 Hz, 2H), 3.50 (d, *J*=1.1 Hz, 2H), 3.46 (d, *J*=6.4 Hz, 2H), 2.89–2.59 (m, 3H), 1.82 (dt, *J*=8.9, 1.5 Hz, 1H), 1.64 (d, *J*=8.9 Hz, 1H); MS (ESI) calcd for $C_{44}H_{38}N_9O_8$ $(M+H)^+$ 820.3, found 820.2.

IWR1-TP2-Poma

10.2 mg, 76% yield. ^{1}H NMR (400 MHz, $CDCl_3$) δ 10.71 (s, 1H), 8.92 (dd, *J*=7.4, 1.6 Hz, 1H), 8.72 (d, *J*=4.4 Hz, 1H), 8.25 (s, 1H), 8.14–8.07 (m, 2H), 7.69–7.57 (m, 3H), 7.43–7.34 (m, 3H), 7.03 (dd, *J*=5.9, 3.7 Hz, 2H), 6.81 (d, *J*=8.5 Hz, 1H), 6.29 (t, *J*=1.9 Hz, 2H), 6.01 (s, 2H), 4.87 (dd, *J*=12.0, 5.4 Hz, 1H), 4.71 (s, 2H), 3.70 (dd, *J*=5.9, 3.2 Hz, 2H), 3.66–3.60 (m, 4H), 3.54 (dq, *J*=3.5, 1.7 Hz, 2H), 3.49 (d, *J*=1.6 Hz, 4H), 3.35 (t, *J*=5.3 Hz, 2H), 2.97–2.64 (m, 3H), 1.82 (dt, *J*=8.9, 1.7 Hz, 1H), 1.64 (d, *J*=8.7 Hz, 1H); MS (ESI) calcd for $C_{46}H_{42}N_9O_9$ $(M+H)^+$ 864.3, found 864.3.

IWR1-TP3-Poma

11.0 mg, 95% yield. ^{1}H NMR (400 MHz, $CDCl_3$) δ 10.74 (s, 1H), 8.93 (dd, *J*=6.1, 2.8 Hz, 1H), 8.78 (d, *J*=4.4 Hz, 1H), 8.55 (s, 1H), 8.15–8.06 (m, 2H), 7.70–7.58 (m, 3H), 7.44 (dd, *J*=8.5, 7.1 Hz, 1H), 7.40–7.35 (m, 2H), 7.09 (d, *J*=4.4 Hz, 1H), 7.05 (d, *J*=7.1 Hz, 1H), 6.84 (d, *J*=8.5 Hz, 1H), 6.29 (t, *J*=1.9 Hz, 2H), 6.01 (s, 2H), 4.93–4.85 (m, 1H), 4.70 (s, 2H), 3.76–3.59 (m, 10H), 3.54 (dq, *J*=3.4, 1.6 Hz, 2H), 3.49 (dd, *J*=3.0, 1.6 Hz, 2H), 3.39 (t, *J*=5.2 Hz, 2H), 2.95–2.66 (m, 3H), 2.10 (td, *J*=9.8, 9.0, 3.3 Hz, 1H), 1.82 (dt, *J*=8.9, 1.7 Hz, 1H), 1.65 (d, *J*=8.7 Hz, 1H); MS (ESI) calcd for $C_{48}H_{46}N_9O_{10}$ $(M+H)^+$ 908.3, found 908.3.

IWR1-TP5-Poma

7.6 mg, 78% yield. ^{1}H NMR (400 MHz, $CDCl_3$) δ 10.76 (s, 1H), 8.95 (dd, *J*=7.5, 1.4 Hz, 1H), 8.77 (d, *J*=4.4 Hz, 1H), 8.51 (s, 1H), 8.15–8.06 (m, 2H), 7.77–7.62 (m, 3H), 7.46 (dd, *J*=8.5, 7.1 Hz, 1H), 7.42–7.33 (m, 2H), 7.21–7.14 (m, 2H), 7.10–7.03 (m, 2H), 6.87 (d, *J*=8.5 Hz, 1H), 6.29 (t, *J*=1.8 Hz, 2H), 6.03 (s, 2H), 4.88 (dd, *J*=11.9, 5.4 Hz, 1H), 4.68 (s, 2H), 3.75–3.58 (m, 18H), 3.54 (dq, *J*=3.4, 1.7 Hz, 2H), 3.48 (dd, *J*=3.0, 1.6 Hz, 2H), 3.41 (t, *J*=5.2 Hz, 2H), 2.91–2.63 (m, 3H), 2.10 (dt, *J*=10.5, 4.1 Hz, 1H), 1.82 (dt, *J*=8.9, 1.7 Hz, 1H), 1.65 (dd, *J*=8.8, 1.6 Hz, 1H); MS (ESI) calcd for $C_{52}H_{54}N_9O_{12}$ $(M+H)^+$ 996.4, found 996.4.

IWR1-TP6-Poma

13.1 mg, 91% yield. ^{1}H NMR (400 MHz, $CDCl_3$) δ 10.75 (s, 1H), 8.94 (d, *J*=7.5 Hz, 1H), 8.77 (d, *J*=4.3 Hz, 1H), 8.61 (s, 1H), 8.11 (d, *J*=8.4 Hz, 2H), 7.84–7.60 (m, 3H), 7.44 (dd, *J*=8.5, 7.2 Hz, 1H), 7.37 (d, *J*=8.3 Hz, 2H), 7.06 (dd, *J*=9.4, 5.7 Hz, 2H), 6.86 (d, *J*=8.5 Hz, 1H), 6.29 (t, *J*=1.9 Hz, 2H), 6.04 (s, 2H), 4.88 (dd, *J*=11.7, 5.4 Hz, 1H), 4.69 (s, 2H), 3.68 (t, *J*=5.1 Hz, 4H), 3.64–3.56 (m, 20H), 3.55–3.51 (m, 2H), 3.48 (d, *J*=2.1 Hz, 2H), 3.41 (t, *J*=5.3 Hz, 2H), 2.89–2.69 (m, 3H), 2.14–2.04 (m, 1H), 1.85–1.77 (m, 1H), 1.64 (d, *J*=8.9 Hz, 1H); MS (ESI) calcd for $C_{54}H_{58}N_9O_{13}$ $(M+H)^+$ 1040.4, found 1040.4.

Synthesis of IWR1-P(n)-Poma

To a solution of [*2472645-01-3*] (***Zhang et al., 2019***) (1.0 equiv) in methylene chloride was added amino-PEG(n)-pomalidomide (1.05 equiv) followed by 4 Å molecular sieves. After stirring at 23°C overnight, sodium triacetoxyborohydride (20 equiv) was added and the reaction was stirred for 4 h before quenched with water. The mixture was extracted with methylene chloride for three times. The combined organic layers were washed with brine, dried over sodium sulfate, concentrated, and

purified by silica gel flash column chromatography followed by preparative HPLC to give IWR1-P(n)-Poma as a yellow solid.

IWR1-P1-Poma

16.0 mg, 78% yield. ^{1}H NMR (500 MHz, $CDCl_3$) δ 10.48 (s, 1H), 9.09 (s, 1H), 8.67 (t, *J*=6.1 Hz, 2H), 7.97 (d, *J*=8.1 Hz, 2H), 7.55 (d, *J*=8.5 Hz, 2H), 7.43 (t, *J*=8.0 Hz, 1H), 7.36 (t, *J*=7.7 Hz, 1H), 7.32 (d, *J*=8.1 Hz, 2H), 6.96 (d, *J*=7.1 Hz, 1H), 6.76 (d, *J*=8.6 Hz, 1H), 6.27 (t, *J*=1.9 Hz, 2H), 4.74 (dd, *J*=13.1, 5.3 Hz, 1H), 4.59 (s, 2H), 3.74 (s, 2H), 3.62 (t, *J*=5.0 Hz, 2H), 3.54–3.49 (m, 2H), 3.47 (s, 4H), 3.34 (d, *J*=5.6 Hz, 2H), 3.28–3.19 (m, 2H), 2.79–2.38 (m, 3H), 1.93 (d, *J*=12.4 Hz, 1H), 1.80 (dt, *J*=8.9, 1.7 Hz, 1H), 1.63 (d, *J*=8.8 Hz, 1H); MS (ESI) calcd for $C_{43}H_{40}N_7O_8$ $(M+H)^+$ 782.3, found 782.2.

IWR1-P2-Poma

13.1 mg, 56% yield. ^{1}H NMR (500 MHz, $CDCl_3$) δ 10.53 (s, 1H), 9.39–9.14 (m, 1H), 8.71 (dd, *J*=23.5, 5.9 Hz, 2H), 8.12–7.91 (m, 2H), 7.60 (t, *J*=7.4 Hz, 2H), 7.49 (t, *J*=8.2 Hz, 1H), 7.36 (d, *J*=8.0 Hz, 2H), 7.32–7.23 (m, 2H), 7.16 (dd, *J*=12.7, 7.1 Hz, 1H), 6.95 (d, *J*=7.0 Hz, 1H), 6.60 (d, *J*=8.5 Hz, 1H), 6.29 (t, *J*=1.9 Hz, 2H), 4.91 (dd, *J*=12.7, 5.4 Hz, 1H), 4.69 (s, 2H), 3.85 (t, *J*=4.8 Hz, 2H), 3.68 (d, *J*=4.3 Hz, 3H), 3.63 (dt, *J*=10.2, 4.1 Hz, 4H), 3.58–3.45 (m, 6H), 3.39 (s, 2H), 3.22 (t, *J*=5.1 Hz, 2H), 2.85–2.67 (m, 2H), 2.62 (td, *J*=12.8, 4.7 Hz, 1H), 2.08–1.96 (m, 1H), 1.82 (dt, *J*=9.0, 1.8 Hz, 1H), 1.65 (d, *J*=8.8 Hz, 1H); MS (ESI) calcd for $C_{45}H_{44}N_7O_9$ $(M+H)^+$ 826.3, found 826.3.

IWR1-P3-Poma

13.2 mg, 72% yield. ^{1}H NMR (500 MHz, $CDCl_3$) δ 10.65 (s, 1H), 9.23 (s, 1H), 8.83 (d, *J*=7.6 Hz, 1H), 8.75 (d, *J*=4.0 Hz, 1H), 8.10–8.01 (m, 2H), 7.66 (t, *J*=7.3 Hz, 2H), 7.56 (t, *J*=8.2 Hz, 1H), 7.45–7.31 (m, 3H), 7.00 (d, *J*=7.1 Hz, 1H), 6.74 (d, *J*=8.6 Hz, 1H), 6.29 (d, *J*=1.8 Hz, 2H), 4.92–4.82 (m, 1H), 4.69 (s, 2H), 3.79 (s, 2H), 3.67–3.51 (m, 14H), 3.51–3.43 (m, 4H), 3.28 (s, 2H), 2.89–2.59 (m, 3H), 2.05 (q, *J*=9.1, 7.1 Hz, 1H), 1.85–1.77 (m, 1H), 1.64 (d, *J*=8.9 Hz, 1H); MS (ESI) calcd for $C_{47}H_{48}N_7O_{10}$ $(M+H)^+$ 870.3, found 870.3.

IWR1-P4-Poma

15.6 mg, 68% yield. ^{1}H NMR (500 MHz, $CDCl_3$) δ 10.66 (s, 1H), 9.02 (s, 1H), 8.85 (d, *J*=7.7 Hz, 1H), 8.76 (d, *J*=3.9 Hz, 1H), 8.07 (d, *J*=8.2 Hz, 2H), 7.77–7.65 (m, 2H), 7.56 (t, *J*=8.1 Hz, 1H), 7.36 (d, *J*=8.0 Hz, 2H), 7.32 (t, *J*=7.8 Hz, 1H), 6.97 (d, *J*=7.0 Hz, 1H), 6.64 (d, *J*=8.5 Hz, 1H), 6.29 (d, *J*=2.0 Hz, 2H), 4.87 (q, *J*=5.7 Hz, 1H), 4.71 (s, 2H), 3.80 (s, 2H), 3.68–3.40 (m, 22H), 3.32 (s, 2H), 3.11 (d, *J*=5.3 Hz, 2H), 2.88–2.58 (m, 3H), 2.12–2.00 (m, 1H), 1.81 (d, *J*=8.9 Hz, 1H), 1.64 (d, *J*=8.8 Hz, 1H); MS (ESI) calcd for $C_{49}H_{52}N_7O_{11}$ $(M+H)^+$ 914.4, found 914.3.

IWR1-P5-Poma

13.6 mg, 53% yield. ^{1}H NMR (500 MHz, $CDCl_3$) δ 10.72 (s, 1H), 8.89 (d, *J*=7.7 Hz, 1H), 8.86 (s, 2H), 8.81 (d, *J*=4.1 Hz, 1H), 8.10 (d, *J*=8.0 Hz, 2H), 7.74 (dd, *J*=13.1, 6.4 Hz, 2H), 7.60 (t, *J*=8.1 Hz, 1H), 7.37 (dd, *J*=8.4, 3.9 Hz, 3H), 7.24 (d, *J*=7.6 Hz, 1H), 7.16 (dd, *J*=12.6, 7.1 Hz, 1H), 7.01 (d, *J*=7.1 Hz, 1H), 6.74 (d, *J*=8.5 Hz, 1H), 6.29 (d, *J*=1.9 Hz, 2H), 4.99–4.83 (m, 1H), 4.75 (s, 2H), 3.80 (s, 2H), 3.70–3.41 (m, 24H), 3.32 (s, 2H), 3.26 (t, *J*=4.2 Hz, 2H), 2.76 (ddd, *J*=61.7, 10.7, 4.5 Hz, 3H), 2.08 (dq, *J*=7.6, 4.1, 2.7 Hz, 1H), 1.81 (d, *J*=9.0 Hz, 1H), 1.64 (d, *J*=8.8 Hz, 1H); MS (ESI) calcd for $C_{51}H_{56}N_7O_{12}$ $(M+H)^+$ 958.4, found 958.4.

IWR1-P6-Poma

9.2 mg, 40% yield. ^{1}H NMR (500 MHz, $CDCl_3$) δ 10.74 (s, 1H), 8.90 (d, *J*=7.5 Hz, 2H), 8.83 (d, *J*=4.1 Hz, 1H), 8.11 (d, *J*=7.9 Hz, 2H), 7.76 (dd, *J*=11.8, 6.5 Hz, 2H), 7.60 (t, *J*=8.1 Hz, 1H), 7.38 (dd, *J*=8.6, 2.2 Hz, 3H), 7.02 (d, *J*=7.1 Hz, 1H), 6.73 (d, *J*=8.5 Hz, 1H), 6.29 (t, *J*=1.8 Hz, 2H), 4.89 (q, *J*=5.5, 5.1 Hz, 1H), 4.77 (t, *J*=9.9 Hz, 2H), 3.83 (s, 2H), 3.68–3.44 (m, 28H), 3.35 (s, 2H), 3.28 (d, *J*=5.1 Hz, 2H), 2.93–2.62 (m, 3H), 2.18–2.01 (m, 1H), 1.85–1.79 (m, 1H), 1.65 (d, *J*=8.9 Hz, 1H); MS (ESI) calcd for $C_{53}H_{60}N_7O_{13}$ $(M+H)^+$ 1002.4, found 1002.4.

Synthesis of IWR1-P(n)-VHL

Prepared as a white powder using the same method as described for IWR1-P(n)-Poma using amino-PEG(n)-VH032 derivatives (***Bond et al., 2020***) with different PEG chain lengths.

IWR1-P1-VHL

2.4 mg, 9% yield. ^{1}H NMR (400 MHz, $CDCl_3$) δ 10.75 (s, 1H), 8.97 (d, *J*=7.7 Hz, 1H), 8.83 (d, *J*=4.4 Hz, 1H), 8.75 (s, 1H), 8.20–8.00 (m, 2H), 7.89 (d, *J*=4.5 Hz, 1H), 7.84 (d, *J*=8.6 Hz, 1H), 7.71 (t, *J*=8.1 Hz, 1H), 7.41–7.32 (m, 2H), 7.29 (s, 4H), 6.66 (d, *J*=8.7 Hz, 1H), 6.29 (t, *J*=1.9 Hz, 2H), 4.92 (s, 2H), 4.68–4.43 (m, 4H), 4.28 (dd, *J*=15.2, 5.2 Hz, 1H), 4.02 (d, *J*=11.4 Hz, 1H), 3.87 (s, 1H), 3.76 (s, 3H), 3.59 (d, *J*=11.0 Hz, 1H), 3.55 (s, 3H), 3.49 (t, *J*=2.3 Hz, 2H), 3.30 (q, *J*=18.2, 15.0 Hz, 5H), 2.49 (s, 3H), 1.82 (d, *J*=8.9 Hz, 1H), 1.65 (d, *J*=9.0 Hz, 2H), 0.96 (s, 9H); MS (ESI) calcd for $C_{53}H_{59}N_8O_8S$ $(M+H)^+$ 967.4, found 967.4.

IWR1-P2-VHL

5.3 mg, 18% yield. ^{1}H NMR (400 MHz, $CDCl_3$) δ 10.76 (t, *J*=2.8 Hz, 1H), 8.96 (q, *J*=4.6, 3.7 Hz, 2H), 8.85 (q, *J*=3.2, 2.3 Hz, 1H), 8.10 (dt, *J*=8.7, 2.7 Hz, 2H), 7.99–7.58 (m, 5H), 7.42–7.33 (m, 4H), 7.31 (t, *J*=2.8 Hz, 2H), 7.02 (d, *J*=8.6 Hz, 1H), 6.47–6.13 (m, 2H), 4.90 (d, *J*=5.4 Hz, 2H), 4.58 (td, *J*=19.0, 16.8, 11.0 Hz, 5H), 4.31 (dd, *J*=12.0, 8.0 Hz, 1H), 3.99 (d, *J*=11.2 Hz, 1H), 3.85 (s, 3H), 3.70–3.60 (m, 7H), 3.55 (s, 3H), 3.50 (t, *J*=3.2 Hz, 4H), 3.37–3.23 (m, 3H), 2.61–2.36 (m, 6H), 2.25 (d, *J*=26.9 Hz, 3H), 1.82 (d, *J*=9.0 Hz, 1H), 1.70–1.53 (m, 1H), 1.32 (td, *J*=7.3, 3.4 Hz, 4H), 0.97 (d, *J*=3.0 Hz, 10H); MS (ESI) calcd for $C_{55}H_{63}N_8O_9S$ $(M+H)^+$ 1011.4, found 1011.4.

IWR1-P3-VHL

4.7 mg, 23% yield. ^{1}H NMR (400 MHz, $CDCl_3$) δ 10.76 (s, 1H), 9.15 (s, 1H), 8.96 (d, *J*=7.5 Hz, 1H), 8.89 (d, *J*=4.1 Hz, 1H), 8.10 (dd, *J*=8.6, 2.1 Hz, 2H), 7.95–7.87 (m, 1H), 7.79 (d, *J*=8.6 Hz, 1H), 7.70 (t, *J*=8.2 Hz, 1H), 7.38 (d, *J*=7.9 Hz, 4H), 7.32 (d, *J*=7.7 Hz, 2H), 6.29 (s, 2H), 4.91 (s, 2H), 4.76–4.39 (m, 4H), 3.86 (s, 2H), 3.80–3.41 (m, 17H), 3.37–3.13 (m, 2H), 2.54 (d, *J*=2.0 Hz, 3H), 2.43 (s, 2H), 2.27 (s, 2H), 1.82 (d, *J*=8.9 Hz, 1H), 1.65 (d, *J*=8.8 Hz, 1H), 1.37–1.29 (m, 3H), 0.96 (s, 9H); MS (ESI) calcd for $C_{57}H_{67}N_8O_{10}S$ $(M+H)^+$ 1055.5, found 1055.4.

IWR1-P4-VHL

3.3 mg, 32% yield. ^{1}H NMR (400 MHz, $CDCl_3$) δ 10.72 (s, 1H), 8.89 (d, *J*=7.7 Hz, 1H), 8.85–8.77 (m, 2H), 8.02 (d, *J*=8.2 Hz, 2H), 7.81 (dd, *J*=20.6, 6.6 Hz, 2H), 7.61 (t, *J*=8.1 Hz, 1H), 7.36–7.23 (m, 6H), 6.91 (d, *J*=10.9 Hz, 1H), 6.21 (t, *J*=1.9 Hz, 2H), 4.81 (s, 2H), 4.66–4.18 (m, 5H), 3.82 (d, *J*=20.1 Hz, 3H), 3.65–3.37 (m, 23H), 3.25 (s, 2H), 2.46 (s, 3H), 1.75 (d, *J*=8.7 Hz, 1H), 1.57 (d, *J*=8.9 Hz, 1H), 1.29 (t, *J*=7.0 Hz, 3H), 0.86 (s, 9H); MS (ESI) calcd for $C_{59}H_{71}N_8O_{11}S$ $(M+H)^+$ 1099.5, found 1099.5.

IWR1-P5-VHL

6.9 mg, 32% yield. ^{1}H NMR (400 MHz, $CDCl_3$) δ 10.70 (s, 1H), 8.94 (s, 1H), 8.90 (d, *J*=7.7 Hz, 1H), 8.82 (d, *J*=4.0 Hz, 1H), 8.04 (d, *J*=8.1 Hz, 2H), 7.88–7.85 (m, 1H), 7.76 (d, *J*=8.6 Hz, 1H), 7.63 (t, *J*=8.1 Hz, 1H), 7.30 (dd, *J*=12.7, 7.1 Hz, 7H), 6.22 (d, *J*=2.2 Hz, 2H), 4.85 (s, 2H), 4.72–4.35 (m, 4H), 4.27 (d, *J*=15.0 Hz, 1H), 3.82 (s, 2H), 3.72–3.28 (m, 21H), 3.24 (d, *J*=7.6 Hz, 3H), 2.46 (s, 3H), 1.75 (d, *J*=8.9 Hz, 1H), 1.58 (d, *J*=8.9 Hz, 1H), 1.28 (t, *J*=6.8 Hz, 3H), 0.88 (s, 9H); MS (ESI) calcd for $C_{61}H_{75}N_8O_{12}S$ $(M+H)^+$ 1143.5, found 1143.4.

IWR1-P6-VHL

6.7 mg, 20% yield. ^{1}H NMR (400 MHz, $CDCl_3$) δ 10.71 (s, 1H), 9.02 (s, 1H), 8.90 (d, *J*=7.7 Hz, 1H), 8.83 (d, *J*=4.3 Hz, 1H), 8.10–7.99 (m, 2H), 7.86 (d, *J*=4.4 Hz, 1H), 7.76 (d, *J*=8.5 Hz, 1H), 7.64 (t, *J*=8.1 Hz, 1H), 7.38–7.25 (m, 7H), 6.22 (t, *J*=1.9 Hz, 2H), 4.87 (s, 2H), 4.50 (ddd, *J*=35.0, 24.8, 16.4 Hz, 4H), 4.27 (dd, *J*=15.2, 4.9 Hz, 1H), 4.02 (d, *J*=11.3 Hz, 1H), 3.82 (d, *J*=5.4 Hz, 2H), 3.68–3.38 (m, 32H), 3.27 (d, *J*=7.3 Hz, 2H), 2.47 (s, 3H), 1.75 (dt, *J*=9.0, 1.7 Hz, 1H), 1.58 (d, *J*=8.9 Hz, 1H), 1.30 (t, *J*=7.0 Hz, 3H), 0.89 (s, 9H); MS (ESI) calcd for $C_{63}H_{79}N_8O_{13}S$ $(M+H)^+$ 1187.5, found 1187.5.

Synthesis of IWR6-P(n)-Poma and IWR6-P(n)-VHL

Prepared using the same methods as described for IWR1-P(n)-Poma and IWR1-P(n)-VHL using [*1801530-64-2*] (**Hrast et al., 2017**).

Synthesis of IWR1-C6-Poma

Prepared using the same methods as described for IWR1-P(n)-Poma using [*2093386-50-4*] (**Li et al., 2019**). MS (ESI) calcd for $C_{45}H_{44}N_7O_7$ $(M+H)^+$ 794.3, found 794.3.

Synthesis of IWR1-R-OLena

To a solution of [*2472645-01-3*] (**Zhang et al., 2019**) (40 mg, 0.09 mmol, 1.0 equiv) in methylene chloride (0.5 mL) was added [*852180-47-3*] (**Kang et al., 2017**) (28 mg, 0.095 mmol, 1.05 equiv) followed by 4 Å molecular sieves (400 mg). After stirring at 23°C overnight, sodium triacetoxyborohydride (48 mg, 0.23 mmol, 2.5 equiv) was added and the reaction was stirred for 4 h before quenched with water. The mixture was extracted with methylene chloride three times. The combined organic layers were washed with brine, dried over sodium sulfate, concentrated, and purified by silica gel flash column chromatography followed by preparative HPLC to give IWR1-RL (45 mg, 69% yield) as a white powder. ^{1}H NMR (400 MHz, $CDCl_3$) δ 10.82 (s, 1H), 8.89 (d, *J*=7.8 Hz, 1H), 8.78 (dd, *J*=4.4, 1.2 Hz, 1H), 8.16–8.03 (m, 2H), 7.67–7.62 (m, 1H), 7.61–7.53 (m, 2H), 7.41–7.34 (m, 2H), 7.27 (d, *J*=8.0 Hz, 2H), 6.95–6.82 (m, 2H), 6.29 (q, *J*=1.7 Hz, 2H), 4.86 (s, 4H), 4.29 (s, 2H), 3.88 (s, 2H), 3.68–3.36 (m, 8H), 3.13 (t, *J*=5.2 Hz, 4H), 2.04 (d, *J*=1.2 Hz, 4H), 1.81 (dd, *J*=8.9, 1.7 Hz, 1H), 1.64 (d, *J*=8.8 Hz, 1H), 1.48 (d, *J*=1.3 Hz, 9H), 1.25 (td, *J*=7.1, 1.2 Hz, 1H); MS (ESI) calcd for $C_{42}H_{45}N_6O_5$ $(M+H)^+$ 713.3, found 713.4.

To a solution of IWR1-RL (17 mg, 0.024 mmol, 1.0 equiv) in methylene chloride (0.6 mL) was added trifluoroacetic acid (0.3 L). After stirring at 40°C overnight, the reaction mixture was concentrated and redissolved in acetonitrile (0.5 mL) before [*1323407-86-8*] (**Hansen et al., 2020**) (10.8 mg, 0.024 mmol, 1.0 equiv) and *N*,*N*-diisopropylethylamine (13 µL, 0.073 mmol, 3.0 equiv) were added. After stirring at 23°C overnight, water was added, and the reaction mixture was extracted with ethyl acetate three times. The combined organic layers were washed with brine, dried over sodium sulfate, concentrated, and purified by silica gel flash column chromatography to give IWR1-R-OLena (5.5 mg, 23% yield) as a white powder. ^{1}H NMR (400 MHz, CD_3OD) δ 9.00 (d, *J*=4.5 Hz, 1H), 8.90 (dd, *J*=7.3, 1.6 Hz, 1H), 8.22–8.03 (m, 2H), 7.83–7.56 (m, 8H), 7.53–7.39 (m, 7H), 7.31 (dd, *J*=8.1, 0.9 Hz, 1H), 7.16–7.09 (m, 2H), 6.32 (t, *J*=1.9 Hz, 2H), 5.35 (s, 2H), 5.18 (dd, *J*=13.3, 5.2 Hz, 1H), 4.64–4.36 (m, 6H), 3.60 (dd, *J*=3.0, 1.6 Hz, 2H), 3.48 (dq, *J*=3.4, 1.7 Hz, 2H), 2.94 (ddd, *J*=18.5, 13.5, 5.5 Hz, 1H), 2.81 (ddd, *J*=17.6, 4.7, 2.4 Hz, 1H), 2.52 (qd, *J*=13.2, 4.6 Hz, 1H), 2.21 (dtd, *J*=12.7, 5.3, 2.5 Hz, 1H), 1.81 (dt, *J*=8.8, 1.7 Hz, 1H), 1.73 (d, *J*=8.8 Hz, 1H), 1.32 (s, 1H); MS (ESI) calcd for $C_{58}H_{55}N_8O_7$ $(M+H)^+$ 975.4, found 975.4.

Synthesis of G007-LK-based PROTACs

Prepared using the same methods as described for the IWR1-based PROTACs.

Synthesis of IWR1-PEG3-NCT

To a solution of 6-carboxy-NCT (**Dwight and Levin, 2016**) (4.0 mg, 0.0086 mmol, 1.0 equiv) in *N*,*N*-dimethylformamide (1 mL) were added *N*,*N*-diisopropylethylamine (5 µL, 0.025 mmol, 3.0 equiv) and *N*,*N*,*N*′,*N*′-tetramethyl-*O*-(*N*-succinimidyl)uranium tetrafluoroborate (TSTU, 3.0 mg, 0.0010 mmol, 1.2 equiv). After stirring at 23°C for 1 h, propargyl PEG3-amine (1.6 mg, 0.0086 mmol, 1.0 equiv) and *N*,*N*-diisopropylethylamine (2 µL, 0.017 mmol, 2.0 equiv) in *N*,*N*-dimethylformamide (0.5 mL) were added. The reaction mixture was stirred at 23°C for 45 min before concentrated and purified by preparative HPLC to give 6-(propargyl-PEG3-carbamoyl)-NCT (3.5 mg, 56% yield). MS (ESI) calcd for $C_{44}H_{50}N_3O_7$ $(M+H)^+$ 732.4, found 732.3.

To a solution of azido-IWR2 (1.2 mg, 0.0027 mmol, 1.0 equiv) in aqueous acetonitrile (67%, 2.25 mL) was added 6-(propargyl-PEG3-carbamoyl)-NCT (2.0 mg, 0.0027 mmol, 1.1 equiv) and copper powder (1.0 mg, 0.0013 mmol, 0.5 equiv). After stirring at 23°C for 16 h, the reaction mixture was filtered, concentrated, and purified by preparative HPLC to give IWR1-PEG3-NCT (1.0 mg, 31% yield) as a blue solid. ^{1}H NMR (600 MHz, MeOD) δ 8.75 (dd, *J*=15.4, 5.9 Hz, 2H), 8.28 (d, *J*=8.2 Hz, 1H), 8.11–8.08 (m, 1H), 8.05 (d, *J*=8.8 Hz, 2H), 7.85 (d, *J*=8.5 Hz, 1H), 7.78 (s, 1H), 7.57 (t, *J*=8.1 Hz, 1H), 7.42 (d, *J*=8.2 Hz, 1H), 7.38 (d, *J*=8.1 Hz, 1H), 7.07 (d, *J*=4.4 Hz, 1H), 6.53 (s, 1H), 6.34–6.22 (m, 2H), 6.14 (s, 1H),

5.95 (s, 1H), 5.35 (t, *J*=5.0 Hz, 1H), 4.58 (s, 2H), 3.86 (q, *J*=9.2 Hz, 2H), 3.70–3.63 (m, 4H), 3.61 (s, 2H), 3.60–3.56 (m, 4H), 3.49 (t, *J*=5.8 Hz, 2H), 3.47–3.40 (m, 4H), 3.19 (m, 1H), 2.97–2.85 (m, 4H), 2.75–2.64 (m, 2H), 2.61 (d, *J*=7.9 Hz, 2H), 2.52–2.43 (m, 4H), 2.28 (t, *J*=7.4 Hz, 2H), 2.23–2.15 (m, 2H), 2.13 (s, 1H), 2.02 (d, *J*=13.6 Hz, 4H), 1.91–1.84 (m, 2H), 1.70 (s, 4H), 1.60 (d, *J*=5.9 Hz, 4H); MS (ESI) calcd for $C_{70}H_{69}N_9O_{10}$ $(M+H)^+$ 1195.5, found 1196.3.

All materials generated in this study are available from the corresponding author upon reasonable request.

Acknowledgements

We thank Dr. Susan Smith (New York University) for providing 293T-TNKS1/2-DKO cells and FLAG-TNKS1-PD construct, Dr. Mariann Bienz and Dr. Melissa Gammons (MRC Laboratory of Molecular Biology) for 293T-DVL2-GFP/AXIN1-dsRed cells and AXIN1-GFP construct, Dr. Dominic Bernkopf (Friedrich-Alexander University Erlangen-Nürnberg) for GFP-AXIN1 and GFP-AXIN2 constructs. We also thank Dr. Katherine Phelps and Dr. Marcel Mettlen for assistance in immunofluorescence microscopy experiments, Dr. Min Fang in automated liquid dispensing and handling, John Shelton in spheroid sectioning, Qing Ding in TMT labeling, and Dr. Duojia Pan, Dr. Xuewu Zhang, Dr. Michael Cohen (Oregon Health & Science University), and Dr. Mike White (IDEAYA Bioscience) for helpful discussions. This work is supported by National Institutes of Health grant R01 CA269377 (to CC), R35 GM134883 (to YY), and P30 CA142543 (to JWS).

Additional information

Competing interests

Lawrence Lum: L. Lum is an equity holder of Loxo at Lilly. The other authors declare that no competing interests exist.

Funding

Funder	Grant reference number	Author
National Institutes of Health	R01 CA269377	Chuo Chen
National Institutes of Health	R35 GM134883	Yonghao Yu
National Institutes of Health	P30 CA142543	Jerry W Shay

The funders had no role in study design, data collection and interpretation, or the decision to submit the work for publication.

Author contributions

Qian Wang, Data curation, Formal analysis, Validation, Investigation, Visualization, Methodology, Writing – review and editing; Liping Li, Lin You, Shuai Wang, Lei Han, Bingnan Wang, Liping Yao, Data curation, Formal analysis, Validation, Investigation, Methodology, Writing – review and editing; Yesu Addepalli, Yong Lu, Ilgen Mender, Ann M Flusche, Chiho Kim, Nageswari Yarravarapu, Andrew Lemoff, Data curation, Formal analysis, Investigation, Methodology, Writing – review and editing; Lawrence Lum, Conceptualization, Resources, Supervision, Methodology, Writing – review and editing; Jerry W Shay, Yonghao Yu, Conceptualization, Resources, Supervision, Funding acquisition, Methodology, Writing – review and editing; Chuo Chen, Conceptualization, Resources, Data curation, Formal analysis, Supervision, Funding acquisition, Validation, Investigation, Visualization, Methodology, Writing – original draft, Project administration, Writing – review and editing

Author ORCIDs

Shuai Wang https://orcid.org/0000-0002-5432-4970
Yesu Addepalli https://orcid.org/0000-0002-8091-1423
Andrew Lemoff https://orcid.org/0000-0002-4943-0170

Lawrence Lum https://orcid.org/0000-0002-6119-0253
Chuo Chen https://orcid.org/0000-0002-3118-4901

Peer review material

Version of Record:
Reviewer #1 (Public review): https://doi.org/10.7554/eLife.109052.4.sa1
Reviewer #2 (Public review): https://doi.org/10.7554/eLife.109052.4.sa2
Reviewer #3 (Public review): https://doi.org/10.7554/eLife.109052.4.sa3
Reviewer #4 (Public review): https://doi.org/10.7554/eLife.109052.4.sa4
Author response https://doi.org/10.7554/eLife.109052.4.sa5

Reviewed preprint v3
Reviewer #1 (Public review): https://doi.org/10.7554/eLife.109052.3.sa4
Reviewer #2 (Public review): https://doi.org/10.7554/eLife.109052.3.sa3
Reviewer #3 (Public review): https://doi.org/10.7554/eLife.109052.3.sa2
Reviewer #4 (Public review): https://doi.org/10.7554/eLife.109052.3.sa1
Author response: https://doi.org/10.7554/eLife.109052.3.sa0
eLife Assessment https://doi.org/10.7554/eLife.109052.3.sa5

Reviewed preprint v2
Reviewer #1 (Public review): https://doi.org/10.7554/eLife.109052.2.sa4
Reviewer #2 (Public review): https://doi.org/10.7554/eLife.109052.2.sa3
Reviewer #3 (Public review): https://doi.org/10.7554/eLife.109052.2.sa2
Reviewer #4 (Public review): https://doi.org/10.7554/eLife.109052.2.sa1
Author response: https://doi.org/10.7554/eLife.109052.2.sa0
eLife Assessment https://doi.org/10.7554/eLife.109052.2.sa5

Reviewed preprint v1
Reviewer #1 (Public review): https://doi.org/10.7554/eLife.109052.1.sa3
Reviewer #2 (Public review): https://doi.org/10.7554/eLife.109052.1.sa2
Reviewer #3 (Public review): https://doi.org/10.7554/eLife.109052.1.sa1
Author response: https://doi.org/10.7554/eLife.109052.1.sa0
eLife Assessment https://doi.org/10.7554/eLife.109052.1.sa4

Additional files

Supplementary files

MDAR checklist

Data availability

The MS data have been deposited in the MassIVE repository with the dataset identifier MSV000089098.

The following dataset was generated:

Author(s)	Year	Dataset title	Dataset URL	Database and Identifier
Chen C	2022	Tankyrase-induced liquid-to-solid phase transition hinders beta-catenin degradation	https://doi.org/10.25345/C50K26F89	MassIVE, 10.25345/C50K26F89

References

Banani SF, Lee HO, Hyman AA, Rosen MK. 2017. Biomolecular condensates: organizers of cellular biochemistry. *Nature Reviews. Molecular Cell Biology* **18**:285–298. DOI: https://doi.org/10.1038/nrm.2017.7, PMID: 28225081

Baradaran-Heravi A, Balgi AD, Hosseini-Farahabadi S, Choi K, Has C, Roberge M. 2021. Effect of small molecule eRF3 degraders on premature termination codon readthrough. *Nucleic Acids Research* **49**:3692–3708. DOI: https://doi.org/10.1093/nar/gkab194, PMID: 33764477

Behrens J, Jerchow BA, Würtele M, Grimm J, Asbrand C, Wirtz R, Kühl M, Wedlich D, Birchmeier W. 1998. Functional interaction of an axin homolog, conductin, with beta-catenin, APC, and GSK3beta. *Science* **280**:596–599. DOI: https://doi.org/10.1126/science.280.5363.596, PMID: 9554852

Bernkopf DB, Brückner M, Hadjihannas MV, Behrens J. 2019. An aggregon in conductin/axin2 regulates Wnt/β-catenin signaling and holds potential for cancer therapy. *Nature Communications* **10**:4251. DOI: https://doi.org/10.1038/s41467-019-12203-8, PMID: 31534175

Bhardwaj A, Yang Y, Ueberheide B, Smith S. 2017. Whole proteome analysis of human tankyrase knockout cells reveals targets of tankyrase-mediated degradation. *Nature Communications* **8**:2214. DOI: https://doi.org/10.1038/s41467-017-02363-w, PMID: 29263426

Bienz M. 2020. Head-to-tail polymerization in the assembly of biomolecular condensates. *Cell* **182**:799–811. DOI: https://doi.org/10.1016/j.cell.2020.07.037

Bischoff JR, Anderson L, Zhu Y, Mossie K, Ng L, Souza B, Schryver B, Flanagan P, Clairvoyant F, Ginther C, Chan CSM, Novotny M, Slamon DJ, Plowman GD. 1998. A homologue of *Drosophila* aurora kinase is oncogenic and amplified in human colorectal cancers. *The EMBO Journal* **17**:3052–3065. DOI: https://doi.org/10.1093/emboj/17.11.3052, PMID: 9606188

Bond MJ, Chu L, Nalawansha DA, Li K, Crews CM. 2020. Targeted degradation of oncogenic $KRAS^{G12C}$ by VHL-recruiting PROTACs. *ACS Central Science* **6**:1367–1375. DOI: https://doi.org/10.1021/acscentsci.0c00411, PMID: 32875077

Chen B, Dodge ME, Tang W, Lu J, Ma Z, Fan C-W, Wei S, Hao W, Kilgore J, Williams NS, Roth MG, Amatruda JF, Chen C, Lum L. 2009. Small molecule–mediated disruption of Wnt-dependent signaling in tissue regeneration and cancer. *Nature Chemical Biology* **5**:100–107. DOI: https://doi.org/10.1038/nchembio.137

Chirnomas D, Hornberger KR, Crews CM. 2023. Protein degraders enter the clinic - a new approach to cancer therapy. *Nature Reviews. Clinical Oncology* **20**:265–278. DOI: https://doi.org/10.1038/s41571-023-00736-3, PMID: 36781982

Clevers H, Nusse R. 2012. Wnt/β-catenin signaling and disease. *Cell* **149**:1192–1205. DOI: https://doi.org/10.1016/j.cell.2012.05.012, PMID: 22682243

Cook BD, Dynek JN, Chang W, Shostak G, Smith S. 2002. Role for the related poly(ADP-Ribose) polymerases tankyrase 1 and 2 at human telomeres. *Molecular and Cellular Biology* **22**:332–342. DOI: https://doi.org/10.1128/MCB.22.1.332-342.2002, PMID: 11739745

DaRosa PA, Wang Z, Jiang X, Pruneda JN, Cong F, Klevit RE, Xu W. 2015. Allosteric activation of the RNF146 ubiquitin ligase by a poly(ADP-ribosyl)ation signal. *Nature* **517**:223–226. DOI: https://doi.org/10.1038/nature13826, PMID: 25327252

Dauch D, Rudalska R, Cossa G, Nault J-C, Kang T-W, Wuestefeld T, Hohmeyer A, Imbeaud S, Yevsa T, Hoenicke L, Pantsar T, Bozko P, Malek NP, Longerich T, Laufer S, Poso A, Zucman-Rossi J, Eilers M, Zender L. 2016. A MYC-aurora kinase A protein complex represents an actionable drug target in p53-altered liver cancer. *Nature Medicine* **22**:744–753. DOI: https://doi.org/10.1038/nm.4107, PMID: 27213815

de la Roche M, Ibrahim AEK, Mieszczanek J, Bienz M. 2014. LEF1 and B9L shield β-catenin from inactivation by Axin, desensitizing colorectal cancer cells to tankyrase inhibitors. *Cancer Research* **74**:1495–1505. DOI: https://doi.org/10.1158/0008-5472.CAN-13-2682, PMID: 24419084

De Rycker M, Price CM. 2004. Tankyrase polymerization is controlled by its sterile alpha motif and poly(ADP-ribose) polymerase domains. *Molecular and Cellular Biology* **24**:9802–9812. DOI: https://doi.org/10.1128/MCB.24.22.9802-9812.2004, PMID: 15509784

Dow LE, O'Rourke KP, Simon J, Tschaharganeh DF, van Es JH, Clevers H, Lowe SW. 2015. Apc restoration promotes cellular differentiation and reestablishes Crypt homeostasis in colorectal cancer. *Cell* **161**:1539–1552. DOI: https://doi.org/10.1016/j.cell.2015.05.033, PMID: 26091037

Dwight SJ, Levin S. 2016. Scalable regioselective synthesis of rhodamine dyes. *Organic Letters* **18**:5316–5319. DOI: https://doi.org/10.1021/acs.orglett.6b02635, PMID: 27704864

Foronda M, Tarumoto Y, Schatoff EM, Leach BI, Diaz BJ, Zimmerman J, Goswami S, Shusterman M, Vakoc CR, Dow LE. 2019. Tankyrase inhibition sensitizes cells to CDK4 blockade. *PLOS ONE* **14**:e0226645. DOI: https://doi.org/10.1371/journal.pone.0226645, PMID: 31891587

Galdeano C, Gadd MS, Soares P, Scaffidi S, Van Molle I, Birced I, Hewitt S, Dias DM, Ciulli A. 2014. Structure-guided design and optimization of small molecules targeting the protein-protein interaction between the von Hippel-Lindau (VHL) E3 ubiquitin ligase and the hypoxia inducible factor (HIF) alpha subunit with in vitro nanomolar affinities. *Journal of Medicinal Chemistry* **57**:8657–8663. DOI: https://doi.org/10.1021/jm5011258, PMID: 25166285

Gammons M, Bienz M. 2018. Multiprotein complexes governing Wnt signal transduction. *Current Opinion in Cell Biology* **51**:42–49. DOI: https://doi.org/10.1016/j.ceb.2017.10.008, PMID: 29153704

Haikarainen T, Krauss S, Lehtio L. 2014. Tankyrases: structure, function and therapeutic implications in cancer. *Current Pharmaceutical Design* **20**:6472–6488. DOI: https://doi.org/10.2174/1381612820666140630101525, PMID: 24975604

Hansen JD, Correa M, Nagy MA, Alexander M, Plantevin V, Grant V, Whitefield B, Huang D, Kercher T, Harris R, Narla RK, Leisten J, Tang Y, Moghaddam M, Ebinger K, Piccotti J, Havens CG, Cathers B, Carmichael J, Daniel T, et al. 2020. Discovery of CRBN E3 ligase modulator CC-92480 for the treatment of relapsed and

refractory multiple myeloma. *Journal of Medicinal Chemistry* **63**:6648–6676. DOI: https://doi.org/10.1021/acs.jmedchem.9b01928, PMID: 32130004

Hrast M, Rožman K, Jukič M, Patin D, Gobec S, Sova M. 2017. Synthesis and structure–activity relationship study of novel quinazolinone-based inhibitors of MurA. *Bioorganic & Medicinal Chemistry Letters* **27**:3529–3533. DOI: https://doi.org/10.1016/j.bmcl.2017.05.064

Hsiao SJ, Smith S. 2008. Tankyrase function at telomeres, spindle poles, and beyond. *Biochimie* **90**:83–92. DOI: https://doi.org/10.1016/j.biochi.2007.07.012, PMID: 17825467

Huang SMA, Mishina YM, Liu S, Cheung A, Stegmeier F, Michaud GA, Charlat O, Wiellette E, Zhang Y, Wiessner S, Hild M, Shi X, Wilson CJ, Mickanin C, Myer V, Fazal A, Tomlinson R, Serluca F, Shao W, Cheng H, et al. 2009. Tankyrase inhibition stabilizes axin and antagonizes Wnt signalling. *Nature* **461**:614–620. DOI: https://doi.org/10.1038/nature08356

Kampmann SS, Skelton BW, Yeoh GC, Abraham LJ, Lengkeek NA, Stubbs KA, Heath CH, Stewart SG. 2015. The synthesis and fluorescence profile of novel thalidomide analogues. *Tetrahedron* **71**:8140–8149. DOI: https://doi.org/10.1016/j.tet.2015.08.036

Kan W, Enos MD, Korkmazhan E, Muennich S, Chen DH, Gammons MV, Vasishtha M, Bienz M, Dunn AR, Skiniotis G, Weis WI. 2020. Limited dishevelled/Axin oligomerization determines efficiency of Wnt/β-catenin signal transduction. *eLife* **9**:e55015. DOI: https://doi.org/10.7554/eLife.55015, PMID: 32297861

Kang S, Kim YM, Kim RY, Seo MJ, No Z, Nam K, Kim S, Kim J. 2017. Synthesis and structure-activity studies of side chain analogues of the anti-tubercular agent, Q203. *European Journal of Medicinal Chemistry* **125**:807–815. DOI: https://doi.org/10.1016/j.ejmech.2016.09.082, PMID: 27750198

Kulak O, Chen H, Holohan B, Wu X, He H, Borek D, Otwinowski Z, Yamaguchi K, Garofalo LA, Ma Z, Wright W, Chen C, Shay JW, Zhang X, Lum L. 2015. Disruption of Wnt/β-catenin signaling and telomeric shortening are inextricable consequences of tankyrase inhibition in human cells. *Molecular and Cellular Biology* **35**:2425–2435. DOI: https://doi.org/10.1128/MCB.00392-15, PMID: 25939383

Langelier MF, Zandarashvili L, Aguiar PM, Black BE, Pascal JM. 2018. NAD^+ analog reveals PARP-1 substrate-blocking mechanism and allosteric communication from catalytic center to DNA-binding domains. *Nature Communications* **9**:844. DOI: https://doi.org/10.1038/s41467-018-03234-8, PMID: 29487285

Lau T, Chan E, Callow M, Waaler J, Boggs J, Blake RA, Magnuson S, Sambrone A, Schutten M, Firestein R, Machon O, Korinek V, Choo E, Diaz D, Merchant M, Polakis P, Holsworth DD, Krauss S, Costa M. 2013. A novel tankyrase small-molecule inhibitor suppresses APC mutation-driven colorectal tumor growth. *Cancer Research* **73**:3132–3144. DOI: https://doi.org/10.1158/0008-5472.CAN-12-4562, PMID: 23539443

Li N, Zhang Y, Han X, Liang K, Wang J, Feng L, Wang W, Songyang Z, Lin C, Yang L, Yu Y, Chen J. 2015. Poly-ADP ribosylation of PTEN by tankyrases promotes PTEN degradation and tumor growth. *Genes & Development* **29**:157–170. DOI: https://doi.org/10.1101/gad.251785.114, PMID: 25547115

Li Y, Yang J, Aguilar A, McEachern D, Przybranowski S, Liu L, Yang CY, Wang M, Han X, Wang S. 2019. Discovery of MD-224 as a First-in-Class, highly potent, and efficacious proteolysis targeting chimera murine double minute 2 degrader capable of achieving complete and durable tumor regression. *Journal of Medicinal Chemistry* **62**:448–466. DOI: https://doi.org/10.1021/acs.jmedchem.8b00909

Lieu CH, Lenz HJ, Benson AB, Meng X, Kim UI, Kim SH, Kim K, Sung MJ. 2025. A first-in-human dose-escalation phase I study of basroparib, a tankyrase inhibitor, in patients with advanced-stage solid tumors. *Cancer Research Communications* **5**:1771–1778. DOI: https://doi.org/10.1158/2767-9764.CRC-25-0502, PMID: 40964966

Mariotti L, Templeton CM, Ranes M, Paracuellos P, Cronin N, Beuron F, Morris E, Guettler S. 2016. Tankyrase Requires SAM domain-dependent polymerization to support Wnt-β-catenin signaling. *Molecular Cell* **63**:498–513. DOI: https://doi.org/10.1016/j.molcel.2016.06.019, PMID: 27494558

Mariotti L, Pollock K, Guettler S. 2017. Regulation of Wnt/β-catenin signalling by tankyrase-dependent poly(ADP-ribosyl)ation and scaffolding. *British Journal of Pharmacology* **174**:4611–4636. DOI: https://doi.org/10.1111/bph.14038, PMID: 28910490

Martino-Echarri E, Brocardo MG, Mills KM, Henderson BR. 2016. Tankyrase inhibitors stimulate the ability of tankyrases to bind axin and drive assembly of β-catenin degradation-competent axin puncta. *PLOS ONE* **11**:e0150484. DOI: https://doi.org/10.1371/journal.pone.0150484, PMID: 26930278

Matyskiela ME, Lu G, Ito T, Pagarigan B, Lu CC, Miller K, Fang W, Wang NY, Nguyen D, Houston J, Carmel G, Tran T, Riley M, Nosaka L, Lander GC, Gaidarova S, Xu S, Ruchelman AL, Handa H, Carmichael J, et al. 2016. A novel cereblon modulator recruits GSPT1 to the CRL4(CRBN) ubiquitin ligase. *Nature* **535**:252–257. DOI: https://doi.org/10.1038/nature18611, PMID: 27338790

Menon M, Elliott R, Bowers L, Balan N, Rafiq R, Costa-Cabral S, Munkonge F, Trinidade I, Porter R, Campbell AD, Johnson ER, Esdar C, Buchstaller HP, Leuthner B, Rohdich F, Schneider R, Sansom O, Wienke D, Ashworth A, Lord CJ. 2019. A novel tankyrase inhibitor, MSC2504877, enhances the effects of clinical CDK4/6 inhibitors. *Scientific Reports* **9**:201. DOI: https://doi.org/10.1038/s41598-018-36447-4, PMID: 30655555

Morin PJ, Vogelstein B, Kinzler KW. 1996. Apoptosis and APC in colorectal tumorigenesis. *PNAS* **93**:7950–7954. DOI: https://doi.org/10.1073/pnas.93.15.7950, PMID: 8755583

Mygland L, Brinch SA, Strand MF, Olsen PA, Aizenshtadt A, Lund K, Solberg NT, Lycke M, Thorvaldsen TE, Espada S, Misaghian D, Page CM, Agafonov O, Nygård S, Chi NW, Lin E, Tan J, Yu Y, Costa M, Krauss S, et al. 2021. Identification of response signatures for tankyrase inhibitor treatment in tumor cell lines. *iScience* **24**:102807. DOI: https://doi.org/10.1016/j.isci.2021.102807, PMID: 34337362

Nong J, Kang K, Shi Q, Zhu X, Tao Q, Chen YG. 2021. Phase separation of Axin organizes the β-catenin destruction complex. *The Journal of Cell Biology* **220**:e202012112. DOI: https://doi.org/10.1083/jcb.202012112, PMID: 33651074

Norum JH, Skarpen E, Brech A, Kuiper R, Waaler J, Krauss S, Sørlie T. 2018. The tankyrase inhibitor G007-LK inhibits small intestine LGR5$^+$ stem cell proliferation without altering tissue morphology. *Biological Research* **51**:3. DOI: https://doi.org/10.1186/s40659-017-0151-6, PMID: 29316982

Nusse R, Clevers H. 2017. Wnt/β-catenin signaling, disease, and emerging therapeutic modalities. *Cell* **169**:985–999. DOI: https://doi.org/10.1016/j.cell.2017.05.016, PMID: 28575679

Pillay N, Mariotti L, Zaleska M, Inian O, Jessop M, Hibbs S, Desfosses A, Hopkins PCR, Templeton CM, Beuron F, Morris EP, Guettler S. 2022. Structural basis of tankyrase activation by polymerization. *Nature* **612**:162–169. DOI: https://doi.org/10.1038/s41586-022-05449-8, PMID: 36418402

Pollock K, Liu M, Zaleska M, Meniconi M, Pfuhl M, Collins I, Guettler S. 2019. Fragment-based screening identifies molecules targeting the substrate-binding ankyrin repeat domains of tankyrase. *Scientific Reports* **9**:19130. DOI: https://doi.org/10.1038/s41598-019-55240-5

Pronobis MI, Rusan NM, Peifer M. 2015. A novel GSK3-regulated APC:Axin interaction regulates Wnt signaling by driving a catalytic cycle of efficient βcatenin destruction. *eLife* **4**:e08022. DOI: https://doi.org/10.7554/eLife.08022, PMID: 26393419

Ranes M, Zaleska M, Sakalas S, Knight R, Guettler S. 2021. Reconstitution of the destruction complex defines roles of AXIN polymers and APC in β-catenin capture, phosphorylation, and ubiquitylation. *Molecular Cell* **81**:3246–3261.. DOI: https://doi.org/10.1016/j.molcel.2021.07.013

Riccio AA, McCauley M, Langelier MF, Pascal JM. 2016. Tankyrase sterile α motif domain polymerization is required for its role in wnt signaling. *Structure* **24**:1573–1581. DOI: https://doi.org/10.1016/j.str.2016.06.022, PMID: 27499439

Robers MB, Dart ML, Woodroofe CC, Zimprich CA, Kirkland TA, Machleidt T, Kupcho KR, Levin S, Hartnett JR, Zimmerman K, Niles AL, Ohana RF, Daniels DL, Slater M, Wood MG, Cong M, Cheng YQ, Wood KV. 2015. Target engagement and drug residence time can be observed in living cells with BRET. *Nature Communications* **6**:10091. DOI: https://doi.org/10.1038/ncomms10091, PMID: 26631872

Sbodio JI, Lodish HF, Chi NW. 2002. Tankyrase-2 oligomerizes with tankyrase-1 and binds to both TRF1 (telomere-repeat-binding factor 1) and IRAP (insulin-responsive aminopeptidase). *The Biochemical Journal* **361**:451–459. DOI: https://doi.org/10.1042/0264-6021:3610451, PMID: 11802774

Schaefer KN, Bonello TT, Zhang S, Williams CE, Roberts DM, McKay DJ, Peifer M. 2018. Supramolecular assembly of the beta-catenin destruction complex and the effect of Wnt signaling on its localization, molecular size, and activity in vivo. *PLOS Genetics* **14**:e1007339. DOI: https://doi.org/10.1371/journal.pgen.1007339, PMID: 29641560

Schaefer KN, Peifer M. 2019. Wnt/Beta-catenin signaling regulation and a role for biomolecular condensates. *Developmental Cell* **48**:429–444. DOI: https://doi.org/10.1016/j.devcel.2019.01.025, PMID: 30782412

Schatoff EM, Goswami S, Zafra MP, Foronda M, Shusterman M, Leach BI, Katti A, Diaz BJ, Dow LE. 2019. Distinct colorectal cancer-associated APC mutations dictate response to tankyrase inhibition. *Cancer Discovery* **9**:1358–1371. DOI: https://doi.org/10.1158/2159-8290.CD-19-0289, PMID: 31337618

Schmid-Burgk JL, Höning K, Ebert TS, Hornung V. 2016. CRISPaint allows modular base-specific gene tagging using a ligase-4-dependent mechanism. *Nature Communications* **7**:12338. DOI: https://doi.org/10.1038/ncomms12338, PMID: 27465542

Schoumacher M, Hurov KE, Lehár J, Yan-Neale Y, Mishina Y, Sonkin D, Korn JM, Flemming D, Jones MD, Antonakos B, Cooke VG, Steiger J, Ledell J, Stump MD, Sellers WR, Danial NN, Shao W. 2014. Inhibiting Tankyrases sensitizes KRAS-mutant cancer cells to MEK inhibitors via FGFR2 feedback signaling. *Cancer Research* **74**:3294–3305. DOI: https://doi.org/10.1158/0008-5472.CAN-14-0138-T, PMID: 24747911

Schreiber SL. 2021. The rise of molecular glues. *Cell* **184**:3–9. DOI: https://doi.org/10.1016/j.cell.2020.12.020, PMID: 33417864

Schwarz-Romond T, Fiedler M, Shibata N, Butler PJG, Kikuchi A, Higuchi Y, Bienz M. 2007a. The DIX domain of Dishevelled confers Wnt signaling by dynamic polymerization. *Nature Structural & Molecular Biology* **14**:484–492. DOI: https://doi.org/10.1038/nsmb1247

Schwarz-Romond T, Metcalfe C, Bienz M. 2007b. Dynamic recruitment of axin by Dishevelled protein assemblies. *Journal of Cell Science* **120**:2402–2412. DOI: https://doi.org/10.1242/jcs.002956, PMID: 17606995

Sellar RS, Sperling AS, Słabicki M, Gasser JA, McConkey ME, Donovan KA, Mageed N, Adams DN, Zou C, Miller PG, Dutta RK, Boettcher S, Lin AE, Sandoval B, Quevedo Barrios VA, Kovalcik V, Koeppel J, Henderson EK, Fink EC, Yang L, et al. 2022. Degradation of GSPT1 causes TP53-independent cell death in leukemia while sparing normal hematopoietic stem cells. *The Journal of Clinical Investigation* **132**:e153514. DOI: https://doi.org/10.1172/JCI153514, PMID: 35763353

Semenova E, Guerriero ML, Zhang B, Hock A, Hopcroft P, Kadamur G, Afzal AM, Lazic SE. 2021. Flexible fitting of PROTAC concentration-response curves with changepoint gaussian processes. *SLAS Discovery* **26**:1212–1224. DOI: https://doi.org/10.1177/24725552211028142, PMID: 34543136

Shin Y, Brangwynne CP. 2017. Liquid phase condensation in cell physiology and disease. *Science* **357**:eaaf4382. DOI: https://doi.org/10.1126/science.aaf4382, PMID: 28935776

Sowa ST, Vela-Rodríguez C, Galera-Prat A, Cázares-Olivera M, Prunskaite-Hyyryläinen R, Ignatev A, Lehtiö L. 2020. A FRET-based high-throughput screening platform for the discovery of chemical probes targeting the scaffolding functions of human tankyrases. *Scientific Reports* **10**:12357. DOI: https://doi.org/10.1038/s41598-020-69229-y, PMID: 32704068

Spink KE, Polakis P, Weis WI. 2000. Structural basis of the Axin-adenomatous polyposis coli interaction. *The EMBO Journal* **19**:2270–2279. DOI: https://doi.org/10.1093/emboj/19.10.2270, PMID: 10811618

Steinebach C, Sosič I, Lindner S, Bricelj A, Kohl F, Ng YLD, Monschke M, Wagner KG, Krönke J, Gütschow M. 2019. A MedChem toolbox for cereblon-directed PROTACs. *MedChemComm* **10**:1037–1041. DOI: https://doi.org/10.1039/c9md00185a, PMID: 31304001

Thorvaldsen TE, Pedersen NM, Wenzel EM, Schultz SW, Brech A, Liestøl K, Waaler J, Krauss S, Stenmark H. 2015. Structure, dynamics, and functionality of tankyrase inhibitor-induced degradasomes. *Molecular Cancer Research* **13**:1487–1501. DOI: https://doi.org/10.1158/1541-7786.MCR-15-0125, PMID: 26124443

Tian H, Biehs B, Warming S, Leong KG, Rangell L, Klein OD, de Sauvage FJ. 2011. A reserve stem cell population in small intestine renders Lgr5-positive cells dispensable. *Nature* **478**:255–259. DOI: https://doi.org/10.1038/nature10408, PMID: 21927002

Wang H, Lu B, Castillo J, Zhang Y, Yang Z, McAllister G, Lindeman A, Reece-Hoyes J, Tallarico J, Russ C, Hoffman G, Xu W, Schirle M, Cong F. 2016. Tankyrase inhibitor sensitizes lung cancer cells to Endothelial Growth Factor Receptor (EGFR) inhibition via stabilizing angiomotins and inhibiting YAP signaling. *Journal of Biological Chemistry* **291**:15256–15266. DOI: https://doi.org/10.1074/jbc.M116.722967

Wang J, Mouradov D, Wang X, Jorissen RN, Chambers MC, Zimmerman LJ, Vasaikar S, Love CG, Li S, Lowes K, Leuchowius KJ, Jousset H, Weinstock J, Yau C, Mariadason J, Shi Z, Ban Y, Chen X, Coffey RJC, Slebos RJC, et al. 2017. Colorectal cancer cell line proteomes are representative of primary tumors and predict drug sensitivity. *Gastroenterology* **153**:1082–1095. DOI: https://doi.org/10.1053/j.gastro.2017.06.008, PMID: 28625833

Weihs F, Wang J, Pfleger KDG, Dacres H. 2020. Experimental determination of the bioluminescence resonance energy transfer (BRET) Förster distances of NanoBRET and red-shifted BRET pairs. *Analytica Chimica Acta* **6**:100059. DOI: https://doi.org/10.1016/j.acax.2020.100059, PMID: 33392495

Winter GE, Buckley DL, Paulk J, Roberts JM, Souza A, Dhe-Paganon S, Bradner JE. 2015. Phthalimide conjugation as a strategy for in vivo target protein degradation. *Science* **348**:1376–1381. DOI: https://doi.org/10.1126/science.aab1433, PMID: 25999370

Zhang Y, Liu S, Mickanin C, Feng Y, Charlat O, Michaud GA, Schirle M, Shi X, Hild M, Bauer A, Myer VE, Finan PM, Porter JA, Huang SMA, Cong F. 2011. RNF146 is a poly(ADP-ribose)-directed E3 ligase that regulates axin degradation and Wnt signalling. *Nature Cell Biology* **13**:623–629. DOI: https://doi.org/10.1038/ncb2222, PMID: 21478859

Zhang L, Shay JW. 2017. Multiple roles of APC and its therapeutic implications in colorectal cancer. *Journal of the National Cancer Institute* **109**:djw332. DOI: https://doi.org/10.1093/jnci/djw332, PMID: 28423402

Zhang L, Kang X, Lu J, Zhang Y, Wu X, Wu G, Zheng J, Tuladhar R, Shi H, Wang Q, Morlock L, Yao H, Huang LJ, Maire P, Kim J, Williams N, Xu J, Chen C, Zhang CC, Lum L. 2019. Installation of a cancer promoting WNT/SIX1 signaling axis by the oncofusion protein MLL-AF9. *EBioMedicine* **39**:145–158. DOI: https://doi.org/10.1016/j.ebiom.2018.11.039

Zhong L, Ding Y, Bandyopadhyay G, Waaler J, Börgeson E, Smith S, Zhang M, Phillips SA, Mahooti S, Mahata SK, Shao J, Krauss S, Chi N-W. 2016a. The PARsylation activity of tankyrase in adipose tissue modulates systemic glucose metabolism in mice. *Diabetologia* **59**:582–591. DOI: https://doi.org/10.1007/s00125-015-3815-1, PMID: 26631215

Zhong Y, Katavolos P, Nguyen T, Lau T, Boggs J, Sambrone A, Kan D, Merchant M, Harstad E, Diaz D, Costa M, Schutten M. 2016b. Tankyrase inhibition causes reversible intestinal toxicity in mice with a therapeutic index < 1. *Toxicologic Pathology* **44**:267–278. DOI: https://doi.org/10.1177/0192623315621192, PMID: 26692561

Zhong Z, Virshup DM. 2020. Wnt signaling and drug resistance in cancer. *Molecular Pharmacology* **97**:72–89. DOI: https://doi.org/10.1124/mol.119.117978, PMID: 31787618